Cell cycle-dependent S-sulfenyl proteomics uncover a redox switch in p21-CDK feedback governing the proliferation-senescence decision

Julia Vorhauser[1,2], Theodoros I. Roumeliotis[3], Jacky K. Leung[1], David Coupe[1], Lu Yu[3], Kristin Böhlig[4], André Nadler[4], Jyoti S. Choudhary[3], Jörg Mansfeld[1,2]

[1]Division of Cancer Biology, Chester Beatty Laboratories, The Institute of Cancer Research, London, UK

[2]Cell Cycle, Biotechnology Center (BIOTEC), TU Dresden, Dresden, Germany

[3]Functional Proteomics Group, Chester Beatty Laboratories, The Institute of Cancer Research, London, UK

[4]Max Planck Institute of Molecular Cell Biology and Genetics, Dresden, Germany

Lead-contact and corresponding author: jorg.mansfeld@icr.ac.uk

Keywords:

Cell cycle; Proliferation; Cell Cycle Exit; Senescence; CDK2; CDK4; p21; CDKN1A; Reactive Oxygen Species; ROS; Redox; Oxidation, Reduction, S-sulfenylation, Sulfenic Acid; Redox Proteomics

SUMMARY

Cells are constantly exposed to reactive oxygen species (ROS) from both intrinsic and extrinsic sources. ROS influence proliferation and cell fate through cysteine oxidation (S-sulfenylation), but specific targets and mechanisms remain unclear. Here, we use redox proteomics to identify cell cycle-coordinated S-sulfenylation and investigate its role in cell cycle decision-making. We find that oxidation of a single cysteine (C41) on the CDK inhibitor p21 during G2 phase determines whether cells continue to proliferate. Preventing C41 oxidation redirects p21 from CDK4-Cyclin D to CDK2-Cyclin A, affecting a negative feedback loop that regulates p21 stability. When C41 cannot be oxidized in G2, daughter cells inherit more p21 from their mother, which decreases proliferation and induces senescence upon irradiation. We therefore identify a redox switch in a core cell cycle regulator that governs the decision to proliferate or exit the cell cycle and present a cell cycle-resolved S-sulfenyl proteome as a valuable resource.

INTRODUCTION

Reactive oxygen species (ROS) have long been known for their ability to oxidize proteins, lipids, and DNA, negatively impacting cell fate and survival. It is now widely accepted that physiological levels of ROS, particularly membrane-permeant hydrogen peroxide (H_2O_2), act in a concentration-dependent manner as signaling molecules in various cellular responses, including proliferation, differentiation, and stress responses[1]. Most cellular H_2O_2 originates from superoxide anions, which are generated by the mitochondrial electron transport chain and NADPH oxidases, and rapidly converted to H_2O_2 by superoxide dismutases. The main cellular targets of ROS are sulfur-containing amino acids cysteine and methionine in proteins, due to their high abundance and oxidation rate constants compared to lipids and nucleic acids[2]. Because H_2O_2 oxidizes cysteines about four times faster than methionines, reversible cysteine oxidation is thought to play a predominant role in ROS signaling[3].

Upon reaction with H_2O_2, the sulfur of cysteines is first oxidized to a sulfenic acid intermediate (S-sulfenylation, SOH), which can subsequently form intra- or intermolecular disulfide bonds or react with thiol-containing metabolites such as glutathione (glutathionylation) or acetyl coenzyme A (CoAthiolation or CoAlation)[4]. Reversibly oxidized cysteines can be reduced by thioredoxin and glutathione-dependent antioxidant systems, a mechanism that highlights the dynamic nature of physiological oxidation as a reversible posttranslational protein modification (oxPTM) capable of regulating protein activity, localization, stability, and interactions[5].

Cumulative evidence suggests that oxPTMs are tightly linked to cell proliferation. The levels of ROS and sulfenic acids increase during the cell cycle[6–9], indicating coordination between the cell cycle, metabolism and redox control[10]. Upregulation of antioxidant activity or prevention of ROS production delays cells in the G1 phase[6] or S phase[7], while inhibiting antioxidant enzymes prevents progression through mitosis[11,12]. Proteomic studies using differential alkylation protocols or cell-permeant sulfenic acid-specific probes have identified hundreds of oxPTMs in the core cell cycle machinery of murine and human cells[13–15]. However, the timing of oxidation in relation to cell cycle progression and the functional consequences for cell proliferation remain to be determined.

Recent reports highlight that key cell cycle kinases are prime targets of ROS. For example, CoAlation of Aurora A facilitates its homodimerization, leading to T-loop autophosphorylation and timely activation in mitosis[4,16,17]. Additionally, the formation of a heterodimeric disulfide bond between G1 phase cyclin-dependent kinase 4 (CDK4) and Cyclin D attenuates CDK4 activity and slows proliferation in human pulmonary arterial smooth muscle cells and arterial endothelial cells[18]. Furthermore, oxidation of a cysteine close to the activatory T-loop of CDK2 regulates its interaction with T-loop phosphatase and kinase, impacting progression through S phase. The degree of CDK2 oxidation reflects the general increase in total ROS during cell cycle progression, providing a rationale for increased CDK2 activity during the S phase[7]. Elucidating whether proteome-wide changes in oxPTMs during proliferation are coordinated with ROS dynamics in a manner like CDK2, and whether other core cell cycle proteins are targeted by oxidation in a cell cycle-dependent manner, will be crucial for understanding how cell cycle and redox regulation are intertwined.

CDKs drive cell cycle progression, and their regulation either directly or through modulation of their interactions with activators or inhibitors is predicted to have direct consequences for cell fate. The timely activation of CDKs during G1 phase determines whether cells commit to proliferation or exit the cell cycle into quiescence or senescence. The CDK inhibitor p21 (gene name: CDKN1A), which inhibits CDK4/6-Cyclin D, CDK2-Cyclin A/E, and CDK1-Cyclin B1 complexes, plays a critical role in this decision-making[19–21]. Cells entering mitosis with high levels of p21, e.g., due to DNA damage or replication stress, give rise to daughter cells destined for cell cycle arrest. Therefore, p21 levels are tightly controlled before mitosis by a double-negative feedback loop involving CDK2 and the SCF-SKP2 E3 ubiquitin ligase[21,22]. CDK2 phosphorylation of p21 creates a phospho-degron and facilitates recognition by SCF-SKP2, leading to proteasomal degradation of p21[23–25]. It is critical to maintain dynamic negative feedback between the two proteins and thus to prevent unphysiologically high concentrations of p21 during G2 phase, as this has acute consequences for cell fate decision-making. How this balance is achieved, and the molecular mechanism(s) involved, remain unknown.

Here, we employ quantitative sulfenic acid proteomics at 2-hour intervals across the cell cycle to identify 1725 unique S-sulfenylation sites in hTERT immortalized retina pigment epithelial cells (RPE-1). We find that while the overall S-sulfenylation state of the

proteome does not change as cells progress through the cell cycle, individual cysteines are dynamically oxidized with functional consequences for cell proliferation. We focus on p21, which is predominantly oxidized on cysteine 41 (C41) during G2 phase. We show that the redox state of C41 redirects p21 between CDK4-Cyclin D and CDK2-Cyclin A complexes, thereby regulating p21 stability during G2 phase and impacting on the decision between proliferation and cell cycle exit into senescence.

RESULTS

Cell Cycle-Resolved Redox Proteomics Identify Dynamic S-Sulfenylation

To label sulfenylated cysteines in living RPE-1 hTERT cells, we made use of the recently developed probe BTD (Figure S1A)[13,26]. BTD is the fastest sulfenic-acid specific cell-permeant probe to date (1,700 M^{-1} s^{-1}); it covalently labels sulfenic acids and features an alkyne moiety for further functionalization by click chemistry (Figure S1B). To assess sulfenic acids in living cells, BTD was added for one hour and then conjugated to an azide-fluorophore (Az647). This labeling process revealed a strong sulfenic acid signal throughout all cell compartments, including the nucleus and ER/mitochondria-like structures (Figure S1C), indicating ubiquitous sulfenic acids in living RPE-1 cells.

Previous studies, including our own, reported that overall ROS levels increase during the cell cycle[6–8]. To investigate whether elevated ROS levels also determine an increase in sulfenic acids levels, we assessed overall S-sulfenylation during the cell cycle, using BTD labeling combined with flow cytometry. Our findings revealed that cells in the later stages of the cell cycle (S, G2/M) exhibit higher levels of sulfenic acids compared to G1 phase cells (Figure S1D), as previously reported[8,27]. To determine if the oxidation state of the complete proteome or rather individual cysteines follow ROS dynamics, we developed a proteomic approach to identify sulfenic acids in different cell cycle phases.

To this end, RPE-1 cells were synchronized at different cell cycle stages by release from 150 nM palbociclib treatment[28] and sulfenic acids were labeled with BTD for one hour at the indicated time points. Proteins were extracted and BTD-labeled proteins were

biotinylated with azide-Dde-biotin via click chemistry. Proteins were then digested, peptides enriched on streptavidin beads, labelled by tandem-mass-tag probes (TMT[29]) to distinguish cell cycle stages, and eluted via chemical cleavage of the Dde moiety present in azide-biotin. Total proteome samples were collected to normalize S-sulfenylation to changes in protein levels (Figure 1A).

Flow-cytometry analysis of cells used for mass spectrometry (MS) showed high synchronicity between the two biological repeats (Figure 1B), which was confirmed by almost identical changes in total protein abundances of cell cycle proteins CDT1, Cyclin A2, and Geminin in both repeats (Figure S1E). We identified 1,725 S-sulfenylation sites across all time points (Table S1), the highest number detected with BTD in unperturbed living cells thus far. Contrary to the expectations based on our flow cytometry results (Figure S1D), we did not observe an overall increase in S-sulfenylation during the cell cycle when changes of individual sites where normalized to changes in protein abundance (Figure 1C).

We filtered the dataset for oscillating sulfenic acids, as changes in oxidation might indicate functional relevance. We correlated changes of individual sites with model curves peaking in S (5 and 7 hours), G2/M (9, 11, and 13 hours), or G1 (17 and 19 hours) (Table S1), and identified 233 cysteine sites with oxidations either peaking (positive correlation) or falling (negative correlation) during S, G2/M, or G1 phases, respectively (Figure 1D, Table S1). Gene ontology analyses for Biological Process (BP), Molecular Function (MF), and Cellular Compartment (CC) showed that sites highly oxidized in G2/M included several cytoskeletal components and cell cycle proteins such as CFL, IQGAP1, CLASP2, PCM1, KIF23, and p21 (indicated with black line). Most dynamic sites were on proteins located within the cytosol, thus directly exposed to multiple ROS sources, such as the plasma membrane, mitochondria, and ER (Figure 1E, Table S1).

Together, our cell cycle-dependent S-sulfenylation mass spectrometry analyses indicate that the overall oxidation state of the proteome remains constant, with only a fraction of sites displaying dynamic changes typical of cell cycle-regulatory modifications such as phosphorylation.

p21 is Oxidized on C41 During G2 Phase

Among core cell cycle regulators, p21, a potent CDK inhibitor of the CIP/KIP family, exhibited dynamic S-sulfenylation throughout the cell cycle. We confirmed p21 oxidation by treating asynchronous RPE-1 cells with BTD for 2 hours, followed by cell lysis and click chemistry with biotin-azide for subsequent enrichment on streptavidin beads (Figure 2A). Both p21 and the known oxidized protein GAPDH[30] were detected in pull-downs from BTD-treated but not control (DMSO) cells, unlike RPL26, a ribosomal protein without cysteine residues.

Cell cycle-dependent S-sulfenyl proteomics indicated p21 oxidation on C41 with a peak in G2 phase (Figure 1D, Figure 2B). C41 is highly conserved among vertebrates and unique to p21 within the CIP/KIP family (Figure S2A and S2B). p21 is an intrinsically disordered protein and forms a partial alpha helical fold only upon binding of its inhibitory N-terminal domain (amino acids: 9-85) to CDK-Cyclins[31–33]. Analysis of the recent p21-CDK4-cyclin D structure[34] and a p21-CDK2-Cyclin A model[35] showed that C41 is uniquely positioned at the interaction surface between p21 and the CDK-Cyclin complex (Figure 2C, Figure S2C). C41 lies near Cyclin D (4Å), CDK4 (6Å) and Cyclin A (2.7Å) suggesting a role for it in trimeric complex formation (Figures 2D & Figure S2C). A hydrogen bond from C41 to the alpha-helix backbone of p21 suggested that this residue might also contribute to its secondary structure (Figure 2D)[36]. Additionally, the IUPred3 algorithm indicated that p21's N terminus, including C41, could be a redox-sensitive region exhibiting structural order-to-disorder changes upon oxidation (Figure 2E)[37].

To estimate the degree of C41 oxidation during G2 phase, we employed a quantitative differential alkylation-reduction-alkylation MS approach with TMT labels to determine the number of total and oxidized cysteines on p21 (Figure S2D)[15,38]. RPE-1 cells expressing endogenously tagged p21-GFP[21] were synchronized in G2 phase by an 11-hour release from palbociclib treatment (Figure 1B), and p21-GFP was enriched using magnetic beads crosslinked to anti-GFP nanobodies (GFP-binder beads)[39,40]. To determine the propensity of cysteines in p21 to be oxidized upon ROS exposure, we added 10 or 100μM H_2O_2 during cell lysis to samples processed in parallel. Our mass

spectrometry analysis identified peptides containing three out of the five cysteines on p21. C13 showed an average steady-state oxidation of 10%, while C34/C41 exhibited 26% (Figure 2F). Since C34 and C41 reside on the same peptide, we could not discriminate their individual oxidation state. However, as C41 was the only oxidized cysteine identified by BTD proteomics (Figure 2B, Table S1), the oxidation state of the C34/C41 peptide likely relates to C41 alone. Adding 100μM H_2O_2 increased C13 oxidation to 38% and fully oxidized C34/C41 (Figure 2F). Therefore, C41 is likely the most redox-reactive cysteine we identified in p21, as suggested by its higher steady-state oxidation and response to H_2O_2 treatment (Figure 2F).

We conclude that a significant proportion of p21 is oxidized during the G2 phase, potentially impacting on p21 structure and its interactions with CDKs.

Mutating C41 Increases p21 Protein Levels and Impairs Proliferation

We next investigated the impact of C41 oxidation on p21 function. We utilized RPE-1 cells expressing endogenously tagged mRuby-PCNA allowing for cell tracking and cell cycle classification[41]. Both alleles of p21 were previously tagged with GFP at their C termini, facilitating the quantification of p21 expression and p21 purification[21]. Using an ouabain selection-based CRISPR-Cas9 gene-editing approach[42], we mutated C41 to the structurally similar but non-oxidizable serine (C41S) to mimic reduced C41 (Figure S3A). We recovered two homozygous knock-in clones (C41S #1 and C41S #2), which we verified by next-generation sequencing (NGS) to contain identical C41S alleles (Figure S3B).

Next, we used fluorescence microscopy to quantify p21-GFP levels in single cells and to determine the percentage of p21-positive cells. Under unperturbed conditions, only few cells expressed p21-GFP, as expected (Figure 3A)[21]. However, compared to WT (7%), we noticed a mild but significant increase in the percentage of p21-positive cells in both C41S mutants (C41S #1 11%, C41S #2 10%) (Figure 3B), and these cells also expressed slightly higher levels of p21 (Figure S3C). To exclude the possibility that elevated p21 levels in C41S mutants were a consequence of DNA damage and/or p53 (TP53) induction, we stained for the double-strand break marker γH2AX; this did not reveal significant differences between WT and C41S cells (Figure 3C and Figure S3D). Similarly,

monitoring p53 expression by Western blot revealed no difference between WT and C41S cells (Figure S3E).

A key event leading up to the G1/S transition is the phosphorylation of retinoblastoma protein (Rb), first by CDK4/6-Cyclin D and then by CDK2-Cyclins E/A[43–45]. We therefore assessed whether elevated levels of p21-GFP in C41S cells affected Rb phosphorylation on serines 807 and 811 (pRb S807/811), two sites targeted by both CDK-cyclin complexes[46,47]. While no difference was obvious through Western Blot (Figure S3E), when analyzed by more sensitive immunostaining both mutants showed a mild decrease in pRb S807/811-positive cells (Figure 3D), suggesting reduced CDK activities. Accordingly, analysis of cell-cycle phase distribution by quantitative Hoechst 33342 imaging (Figure S3F)[48] suggested that slightly more C41S cells were in G1 phase at the expense of S-phase cells (Figure 3E). In support, both C41S mutants needed about 3.5 hours more than WT cells to complete a cell cycle (Figure 3F).

These small differences in proliferation had dramatic consequences in competitive growth assays, where WT and C41S cells were seeded into the same dish and distinguished by NGS after 12 or 20 days of co-culture (Figure 3G). Already after 12 days, C41S cells represented only 25% of all NGS reads, and they were completely outcompeted by day 20 (<3% for both mutants) (Figure 3G-H).

Together, these data show that under unperturbed conditions p21 levels rise further when C41 oxidation is prevented. This results in a longer cell cycle, presumably because the G1/S transition is impaired, as indicated by reduced pRb staining. While effects may appear minor during monoculture, they become highly detrimental upon co-culture with WT cells, suggesting that aberrant redox regulation of p21 on C41 has severe consequences over time.

p21 Stability and Inheritance is Regulated by Oxidation of C41

The attenuated Rb phosphorylation observed in C41S cells (Figure 3D) prompted us to investigate whether p21 WT and C41S differed in their ability to bind CDK4-Cyclin D and CDK2-Cyclin A complexes. To this end, we prepared lysates of asynchronously growing

WT and C41S cells and pulled down p21-GFP using GFP-binder beads. We did this in the absence of reducing reagents to preserve potential C41 oxidation. Western blot analysis for bound CDK-Cyclin complexes revealed that p21-GFP C41S bound significantly less CDK4-Cyclin D1 than p21-GFP WT, while instead it bound more CDK2 (Figure S4A-D). Interactions of p21 with Cyclin A2, Cyclin B1, and CDK1 were largely comparable between WT and C41S cells (Figure S4E-G). We noticed that, unlike CDK2, Cyclin A2 was not significantly enriched in p21-GFP C41S possibly reflecting the fact that in asynchronous cells CDK2 also binds to Cyclin E and Cyclin A also binds CDK1, and this could reduce the sensitivity of this assay. Importantly, adding the reducing reagent DTT during cell lysis abrogated the differences in CDK4 and CDK2 binding between p21-GFP WT and C41S, indicating that the redox state of C41 rather than unrelated effects of C41S mutagenesis was responsible for changed p21-CDK-Cyclin interactions (Figure S4H-J).
The differences in CDK4 and CDK2 binding between p21-GFP WT and C41S in non-reducing conditions suggest that C41 oxidation directs p21 to CDK4, whereas binding to CDK2 preferentially occurs when C41 is reduced. To test this idea, we synchronized cells in G2 phase, where C41 oxidation was highest (Figure 2B). As in asynchronous cells (Figure S4A), GFP-binder pull-downs confirmed that p21-GFP C41S bound significantly less CDK4 but almost twice as much CDK2 (Figure 4A-C). The addition of 10μM H_2O_2 for 30 minutes before lysis to maximize C41 oxidation further promoted p21-GFP binding to CDK4 in WT but not in C41S cells. In contrast, the interaction with CDK2 was not affected by additional oxidation of p21-GFP (Figure 4A-C).

CDK2-Cyclin A interacts with p21 in two distinct ways: i) through an inhibitory interaction with the N-terminal domain of p21, involving C41, that leads to CDK2 inhibition, and ii) through a kinase-substrate interaction that leads to phosphorylation of p21 on serine 130 (S130), followed by recognition by the SCF-SKP2 ubiquitin ligase, and eventual proteasomal degradation (Figure 4D)[23–25]. Notably, both p21-CDK-Cyclin interactions can occur simultaneously, enabling the degradation of p21 bound in inhibitory p21-CDK-cyclin complexes [24]. The increased inhibitory binding of CDK2 to the N terminus of p21-GFP C41S during G2 phase is therefore predicted to sequester CDK2-cyclin A complexes and lessen SCF-SKP2-dependent degradation of p21[21,22]. To test this hypothesis, we blocked protein translation by adding 50μg/ml cycloheximide (CHX) to G2 phase cells

and monitored p21 levels in total lysates by Western blot (Figure 4E-F). From the decay in p21 signal (Figure S4K), we determined that the half-life of untagged p21 is ~30 minutes as reported previously (Figure 4G)[49]. The half-life of p21-GFP was prolonged to 2.5 hours likely due to the fusion of GFP to its C terminus (Figure 4F-G, S4K). Mutating C41S further stabilized p21-GFP, resulting in a half-life of >5 hours in both C41S cell lines, aligning with the idea that the negative feedback between p21 and CDK2 in these cells is tilted towards CDK2 inhibition (Figure 4F-G, S4K). Remarkably, significant differences in p21-GFP stability between WT and C41S were undetectable in asynchronous cells (Figure S4L), which predominantly consists of cells in G1 phase (Figure 3E), where the SCF-SKP2 degradation mechanism is not active, and of cells in S phase, where p21 is additionally degraded by PCNA-CRL4-CDT2[21,50,51].

The prolonged half-life of p21-GFP C41S during the G2 phase may affect how much p21 mother cells pass on to their daughters, thereby determining whether daughters rapidly continue proliferating or exit from the cell cycle[19–21]. Since in unperturbed conditions C41S mutants showed only a mild increase in p21-positive cells (Figure 3A-B), we turned to quantitative single-cell imaging of hundreds of asynchronously growing cells. Using an advanced analysis pipeline, we automatically segmented, tracked, and classified the cell cycle phase of cells using mRuby-PCNA[41]. This allowed us to computationally align cells at the S/G2 transition (Figure S4M) and extract p21-GFP intensity in single cells from G2 phase, to mitosis, and through the first 8 hours of the daughter G1 phase (Figure S4N). As typical for single-cell data, we observed large degrees of cell-to-cell heterogeneity; however, calculating mean p21-GFP intensities revealed a stronger increase in both C41S mutants during G2 phase compared to WT cells (Figure 4H-I). This increase resulted in a higher amount of p21 being inherited by daughter cells through mitosis (Figure 4J). As anticipated, p21 levels in daughter cell in G1 phase were more variable (Figure 4K).

We conclude that the redox state of C41 regulates the interplay between p21, CDK2, and CDK4, thereby determining p21 stability during G2 phase. When C41 cannot be oxidized, the balance between p21 and CDK2 is tipped towards CDK2, potentially affecting cell

fate decision-making in the subsequent cell cycle as mother cells transmit more p21 to their daughters.

The Redox State of C41 Determines Sensitivity to DNA Damage and p53 Signaling

The prolonged half-life of p21 during G2 phase in C41S cells (Figure 4G) suggests that these mutants should respond more strongly to stresses that upregulate p21 expression. Our single-cell imaging pipeline requires cells to enter mitosis to precisely determine the duration of G2 (Figure S4M), which causes problems when dealing with cells that arrest in G2 phase or skip mitosis after p21-inducing treatments[52–54]. Therefore, we resolved to deriving cell cycle phases from asynchronous cell populations by means of quantitative Hoechst 33342 staining, as previously shown in Figure S3F. Bivariate density plots showing Hoechst 33342 and p21-GFP intensities in unperturbed cells recapitulated the known changes in p21 expression during the cell cycle: high expression in G1 phase, low in S phase, and low with a higher degree of heterogeneity in G2/M (Figure S5A)[21].

Upon receiving a low dose (2Gy) of ionizing radiation and recovering for 24 hours, a population of G2/M cells with high p21 expression emerged and was significantly more prominent in both C41S mutants than in the WT (Figures 5A, B, compared also to Figure S5A). We confirmed this observation by treating cells with 1μM nutlin-3 for 24 hours to induce p21 expression via p53 stabilization independently of DNA damage (Figure 5C)[55]. In typical tissue culture conditions at 21% O_2, RPE-1 cells are continuously exposed to elevated oxygen levels (hyperoxia) compared to their native environment in the retina. To assess the impact of elevated oxygen levels on our model, we decided to confirm our observations in normoxic conditions using a normoxia workstation to grow RPE-1 cells in 6.3% O_2[56,57]. Cells were adapted for five days or more at 6.3% O_2 before the experiment to account for the induction of HIF signaling, which typically lasts for up to 4 days[58,59]. Surprisingly, growth at 6.3% O_2 strongly increased the steady-state levels of p21: whereas at 21% O_2 less than 10% of cells were p21 positive, this fraction increased to over 60% at 6.3% O_2 (Figure S5B, C). The increase in p21 expression was likely due to DNA damage, as over 50% of cells grown at 6.3% O_2 contained γH2AX foci compared to only 11% at 21% O_2 (Figure S5D, E). While the reason for higher DNA damage in RPE-1 cells during normoxic cell culture remains to be investigated, these findings provided us

with an alternative setting to compare the response of WT and C41S cells to p21 induction. Like upon irradiation and nutlin-3 treatment, the number of G2 phase cells with high p21 levels doubled in C41S cells compared to WT (Figure 5D).

Higher levels of p21 (Figure 4I) and increased interaction with CDK2 (Figure 4C) suggest that CDK2 activity is reduced during G2 phase in C41S cells. To investigate this possibility, we monitored pRb S807/811 as a readout of CDK activity in bivariate density plots with Hoechst 33342 after nutlin-3 treatment. Whereas almost no control G2 cells displayed low pRb levels (Figure S5F), upon nutlin-3 treatment this population increased to 5% in WT and 17% and 14% in C41S cells, respectively (Figure 5E, 5F), supporting the hypothesis that overall CDK activity in C41S is reduced during G2 phase. These findings indicate that the redox state of C41 becomes increasingly crucial in response to stresses that upregulate p21 expression.

While we found that under reducing conditions there is no difference in the binding of p21 WT and C41S to either CDK4 or CDK2 (Figure S4H), we wondered if we could provide additional evidence that the redox state of C41, rather than its mutation *per se*, would explain our results thus far. To this end, we made use of a genetically encoded anti-GFP nanobody, VHH4[39], to target an antioxidant enzyme to the C terminus of p21, expecting this would allow us to regulate the redox state of C41 without the need to introduce a mutation. To keep C41 in the reduced state mimicking the C41S mutation, we fused human influenza hemagglutinin tag (HA)-tagged VHH4 to the antioxidant enzyme Thioredoxin 1 (TRX WT). In parallel, we also generated a fusion with an inactive variant of TRX, where both catalytic cysteines (C32 and C35) were mutated to serines (TRX mut) (Figure 5G). As a cellular readout for C41 oxidation, we monitored p21 levels in cells treated with 1μM nutlin-3 for 24 hours as in Figure 5C, predicting that localized reduction of C41 by HA-VHH4-TRX WT, but not by HA-VHH4-TRX mut, would increase the fraction of G2 cells with high p21 levels. To better compare WT and mutant cell lines, we created tetracycline-inducible isogenic stable cell lines taking advantage of the single FRT site and the tetracycline repressor encoded in the genome of p21-GFP cells[21]. We optimized tetracycline induction to express comparable levels of HA-VHH4-TRX WT and HA-VHH4-TRX mut in p21 WT and C41S cells (Figure 5H), and then quantified the percentage of G2

phase cells with high p21 expression from bivariate density plots (Figure S5G, H). We noticed that expression of any VHH4 construct resulted in more cells with higher p21 intensity, and this was expected since the binding of VHH4 to GFP increases GFP fluorescence by about 1.5fold[60] (compare Figures 5C and 5I). Importantly, expressing HA-VHH4-TRX WT significantly increased p21-GFP WT levels further compared to HA-VHH4-TRX mut and thus faithfully phenocopied the effect of non-oxidizable p21-GFP C41S (Figure 5I, Figure S5G). In contrast, expressing HA-VHH4-TRX WT or HA-VHH4-TRX mut did not differentially affect the levels of p21-C41S (Figure 5J, Figure S5H).

Thus, we show that reduced C41 oxidation sensitizes cells to treatments that induce p21 expression, since it prolonged its half-life. p21-targeted expression of the antioxidant TRX recapitulates this observation, demonstrating that p21 stabilization depends on C41 reduction and is not a side effect of mutating C41 to serine.

Non-Oxidizable C41 Primes Cells for Cell Cycle Exit into Senescence

Cells with non-oxidizable C41 pass more p21 on to their daughters (Figure 4J), a trend that becomes particularly pronounced in response to p21-inducing stresses. Since inherited levels of p21 influence the decision between proliferation and cell cycle exit[19–21], we investigated the long-term consequences of lacking C41 oxidation. To this end, we treated WT and C41S cells with increasing doses of ionizing radiation and assessed their fate after six days. Replicating previous short-term responses to radiation (Figure 5A, B), C41S cells accumulated more p21 than WT cells in a dose-dependent manner (Figure 6A). Accordingly, these cells displayed significantly higher numbers of pRb S807/811-negative cells, consistent with cell cycle exit (Figure 6B)[45].

To determine the nature of the cell cycle exit, we stained cells for the senescence marker β-galactosidase and combined it with a nuclear marker to precisely measure β-galactosidase activity per cell[61]. In unperturbed conditions, the level of β-galactosidase activity was similar between WT and C41S cells (Figure 6C-D). However, in response to 4 and 6Gy irradiation followed by a six-day recovery, both C41S mutants exhibited significantly higher β-galactosidase activity compared to WT, indicating that lack of C41 oxidation determines much more frequent cell cycle exit into senescence (Figure 6C-D).

To corroborate this result, we conducted long-term proliferation assays by seeding cells at low density after 6Gy irradiation and staining with crystal-violet once WT cells reached confluency. We observed significantly less crystal-violet staining in C41S compared to WT cells, even without irradiation, in agreement with their prolonged doubling time (Figures 6E-F, Figure 3F). The 6Gy irradiation treatment strongly exacerbated this difference, indicating that the majority of C41S cells had permanently exited the cell cycle and entered senescence (Figures 6E-F).

We conclude that the inability to oxidize C41, and the consequently slower p21 turnover, prime cells for permanent cell cycle exit into senescence. This effect is particularly evident following genotoxic stress that induces p21 expression.

DISCUSSION

ROS levels constantly fluctuate in proliferating cells, primarily due to growth factor-induced NADPH oxidases and mitochondrial oxidative phosphorylation[7,9,62,63]. These changes are expected to alter the oxidation state of the proteome: Rapkine observed already in 1931 that thiol staining of the mitotic spindle in sea urchin eggs peaks during prophase and metaphase and decreases in anaphase[64]. Similarly, sulfenic acids increase from G1 to S and further to G2/M in human cells (Figure S1D)[8,27]. However, the specific thiols oxidized in a cell cycle-dependent manner and the functional consequences of these dynamic oxidations remained unclear.

Cell Cycle-Resolved Dynamics of S-Sulfenylation

Here, we identified 1725 sulfenic acid sites on 1166 proteins across the cell cycle with a 2-hour resolution. In contrast with what flow cytometry analyses proposed (Figure S1D)[8,27] , we found that the normalized sulfenylation state of the total proteome did not change throughout the cell cycle (Figure 1C), suggesting that the fluctuations in the amount of sulfenic acids observed in flow cytometry studies reflect changes in the abundance of proteins during growth, rather than in their redox state. About 13% of the sulfenic acids we identified showed significant cell cycle-dependent dynamics that correlated with G1, S, or G2/M phases (Figure 1D). Changes in the levels of sulfenic acids

were normalized to individual protein levels at each time point, to account for cell cycle-dependent changes in protein expression (Table S1). Gene ontology analysis indicated that proteins involved in cytoskeleton remodeling and the cell cycle are particularly oxidized during G2/M (Figure 1E, Table S1). This implies that dynamic S-sulfenylation might be involved in cortical changes and faithful setup of a mitotic spindle when cells enter mitosis. Indeed, oxidation of IQGAP1 and CFL1 affect cytoskeletal dynamics[65,66], and oxidation-dependent clustering of pericentriolar material 1 (PCM1) inhibits primary cilia formation[67], suggesting consequences for centrosome function as well.

Cell cycle-dependent S-sulfenylation in response to growth factors or metabolic changes may be driven by spatio-temporal co-localization with ROS-producing sources like mitochondria or NADPH oxidases[68,69]. While mitochondrial ROS are predominantly released into the cytoplasm and do not cause damage to nuclear DNA[70], it is conceivable that nuclear proteins become oxidized before nuclear import or are targeted by nuclear sources of ROS (e.g. spermine oxidase)[1]. Indeed, recent findings in *S. cerevisiae* suggest that differential oxidation on proteins is not limited to areas in the proximity of ROS-producing compartments but can also occur in highly differentiated nanoscale regions within subcellular compartments[71]. This aligns with our observations that S-sulfenylation can oscillate on cytoplasmic proteins too (Figure 1D) and even display different behavior between individual cysteines within the same protein (Table S1). Allowing this spatial specificity may rely on the accessibility of cysteines, their chemical propensity for oxidation (pKa), or local pH changes. Alternatively, peroxiredoxin-dependent redox relays[72] and proximity of thiols to phosphorylation sites[73] could translate redox signaling into cell cycle-regulated protein interactions and changes in kinase activity.

p21 Oxidation

Our cell cycle-resolved sulfenic acid proteome identified the CDK inhibitor p21 as a redox-regulated component of the core cell cycle machinery (Figure 2, Table S1). Oxidation of p21 on C41 peaked in the G2 phase, when over 25% of p21 molecules were oxidized on C41 (Figure 2B and 2F). This might be an underestimation, as C41-oxidized p21 appears more prone to degradation in G2 (Figure 4), and we did not inhibit the 26S proteasome in our experiments. Structure of the p21-CDK4-Cyclin D trimer shows that

C41 sits close to C78 of CDK4, a cysteine that is conserved also in CDK6. Although we found no evidence of an intermolecular disulfide stabilizing CDK4/6-Cyclin D interactions with p21, C78 of CDK4 is also oxidized, albeit not in a dynamic way (Table S1). Whether oxidation of C41 is the only functionally relevant cysteine oxidation on p21 remains to be determined. We also identified that 10% of p21 molecules are oxidized on C13. Furthermore, technical limitations in our stoichiometry analysis did not allow us to distinguish between C34 and C41, as they both reside on the same peptide (Figure 2F). However, the BTD proteome indicates that C41, and not C13 or C34, is predominantly oxidized in living RPE-1 cells, and experiments with C41 mutants and p21-targeted TRX suggest that C41 oxidation alone is sufficient to regulate interactions of p21 with CDK2 and CDK4, thereby affecting the proliferative fate of cells (Figures 3-6).

Redox-Regulated Feedback Between p21 and CDK2

Our data suggest that p21 oxidation on C41 promotes interaction with CDK4-Cyclin D, while reduced C41 directs p21 to CDK2-Cyclin A (Figure 4A-C). Free p21 is highly flexible and disordered but undergoes a disorder-to-order transition when binding to CDK2[32]. However, oxidation of C41, as predicted by IUPred3 analysis, likely induces a conformational change that favors p21 interaction with CDK4 and possibly CDK6 over interaction with CDK2. This affects the negative feedback loop that regulates p21 stability through SCF-SKP2-dependent degradation. We propose that the redox state of C41 regulates feedback between p21 and CDK2, allowing cells to degrade p21 during G2 phase and preventing the transmission of excessive p21 to daughter cells, thus avoiding cell cycle exit and senescence (Figure 7). Elevated p21 oxidation in G2 phase may be driven by the cell cycle-dependent increase in mitochondrial ROS, similarly to what we previously observed for CDK2[7], or by local ROS production at sites of DNA damage[74], which would in this way facilitate continued proliferation once the damage is repaired.

Concluding Remarks

In unperturbed cell culture, only a fraction of cells induces p21 expression during G2 phase[21]. This explains why mutant cell lines unable to oxidize C41 display only moderate proliferation defects (Figure 3). However, in competitive conditions or upon p21-inducing genotoxic stress - common in tumorigenesis - the lack of C41 oxidation becomes a

selective disadvantage, forcing cells to stop replicating (Figures 3-6). Modulation of C41 oxidation may thus be crucial in treating hypoxic tumors with quiescent cancer cells that express high levels of p21 and often evade treatment[75]. It is plausible that tumor re-oxygenation[76] or inhibition of antioxidant enzymes could favor C41 oxidation and thus increase p21 turnover[77], potentially priming cells for cell cycle entry and enhancing their sensitivity to radio- and chemotherapy.

Limitations of the study

BTD uniquely labels sulfenic acids within living cells, avoiding false positives that can arise with differential alkylation-reduction approaches due to atmospheric exposure during sample preparation. However, BTD has limitations: sulfenic acids that quickly convert to disulfides, form other thiol linkages or become increasingly oxidized are less accessible to BTD and may thus be underrepresented, which may explain the modest dynamic changes observed in our data. Conversely, long-lived sulfenic acids are potentially overrepresented due to extended labeling periods. Additionally, BTD's covalent interaction with oxidized cysteines could affect protein function. We addressed the latter issue by limiting BTD labeling to one hour, as established in previous studies[13]. To filter for prototypical cell cycle changes in S-sulfenylation, we correlated oxidation changes of individual sites with model profiles recapitulating peaks or falls of oxidation in G1, S and G2/M. Thus, dynamics outside of these categories, such as sites with multiple changes in oxidation across the cell cycle progression, are neglected in our analysis (Table S1). Their functional relevance requires case-by-case investigations as for p21.

Acknowledgments

We thank Kate Carroll for BTD, Alexis Barr for experimental advice and p21-GFP cells, Alex Radzisheuskaya for advice on NGS, and Stefano Pietra for critical reading the manuscript. Christian Zierhut, Max Douglas, and A. Radzisheuskaya for advice on the manuscript, their labs, present and past Mansfeld lab members for technical help and discussions. We acknowledge support by Kai Betteridge and the Light Microscopy and Flow Cytometry Facilities Chelsea (ICR) and BIOTEC (TU Dresden). J.V. was a member of the Dresden Biomedicine and Bioengineering PhD program and J.K.L. receives funding

from the ICR/RM CRUK RadNet Centre of Excellence (grant: A28724). This work was funded by a Cancer Research UK Senior Cancer Research Fellowship to J.M. (RCCSCF-Nov22/100001), the European Research Council (ERC) under the European Union's Horizon 2020 research and innovation program (grants: REDOXCYCLE, 680042 to J.M.; ASYMMEM, GA 758334 to A.N.) T.I.R. and J.S.C. are funded by the CRUK Centre grant with reference number C309/A25144 and A.N. receives support from VolkswagenStiftung within the Life? initiative.

Author contributions

Conceptualization, J.V. and J.M.; Methodology, J.V., T.I.R., L.Y., J.K.L., D.C., J.C. and J.M; Investigation, J.V., T.I.R., L.Y., J.K.L., D.C., and J.M; Resources, K.B. and A.N.; Writing, J.V. and J.M.; Funding acquisition A.N., J.C., and J.M.; Supervision, J.C., A.N., and J.M.

Data availability

Generated plasmids, cell lines and scripts used for data analyses are available from the corresponding author upon request. The mass spectrometry data and plasmids are deposited on the ProteomeXchange Consortium 73§1 and Addgene, respectively, and are publicly available as of the date of publication. Any additional information required to reanalyze the data reported in this paper is available from the lead contact upon request.

Declaration of interests

The authors declare no competing interests.

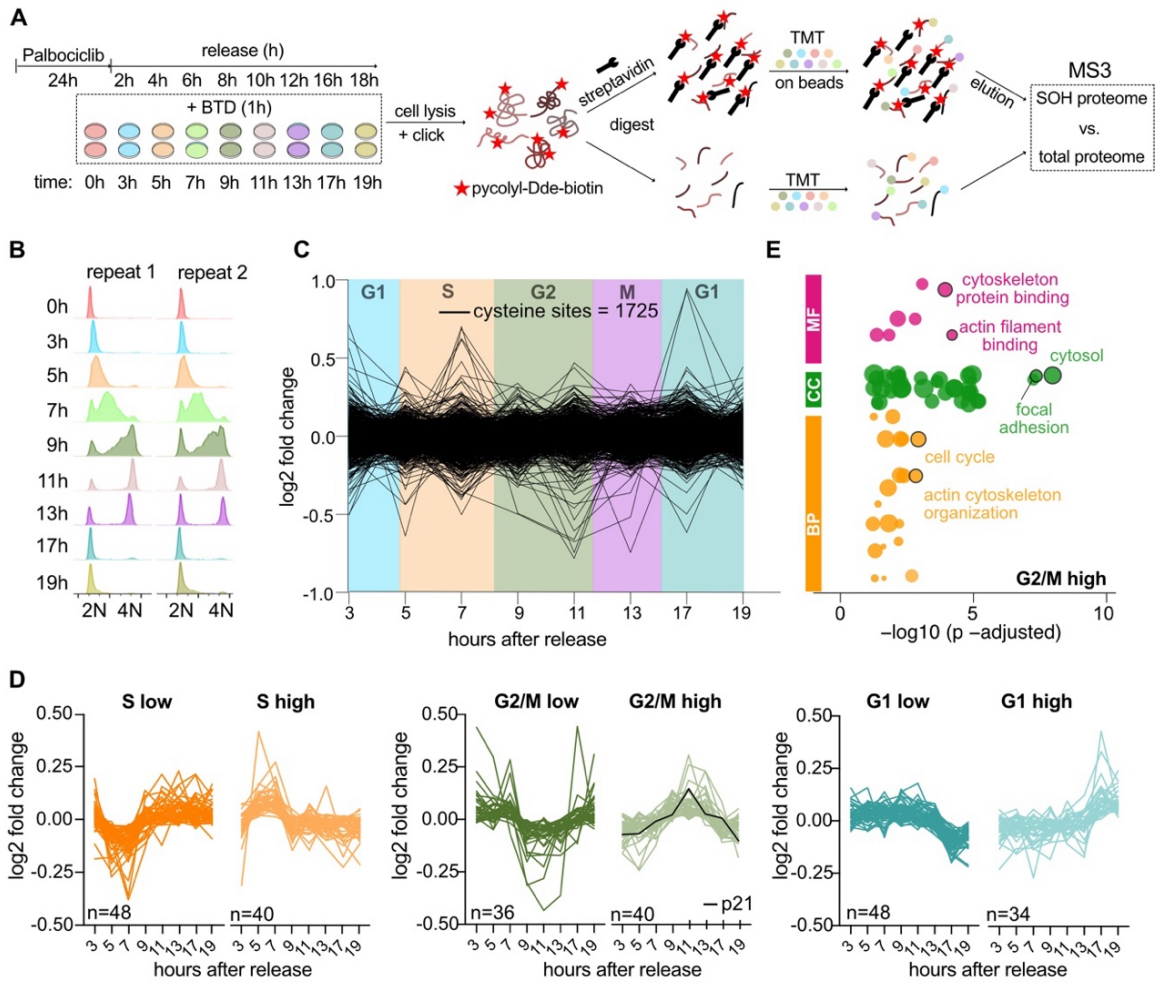

Figure 1. Cell Cycle-Resolved Redox Proteomics Identify Dynamic S-Sulfenylation

(**A**) Proteomics workflow: RPE-1 cells synchronized at different cell cycle stages by release from 24h palbociclib treatment were subjected to BTD labeling, followed by protein extraction, biotinylation via click chemistry, digestion, enrichment, TMT labeling, elution, and mass spectrometry analysis. Total proteome samples were collected in parallel for normalization.

(**B**) Flow cytometric analysis showing the DNA content of cells after BTD incubation used for the two biological repeats, as outlined in (A).

(**C**) Cell cycle-dependent changes of S-sulfenylation across the cell cycle normalized to protein abundance to correct for changes in protein expression. Each line represents a unique oxidized cysteine.

(**D**) Dynamic sulfenic acid sites with significant correlation to prototypical cell cycle oscillations with peaks and valleys in S, G2/M and G1 (see also Table S1). p21 oxidation oscillation is highlighted in black (G2/M high cluster).

(**E**) GO analyses for Biological Process (BP), Molecular Function (MF), and Cellular Component (CC) of dynamic S-sulfenylation sites peaking in G2/M was performed with gProfiler[78]. Note, GO analysis of all other dynamic sites and complete annotation of enriched terms are presented in Table S1.

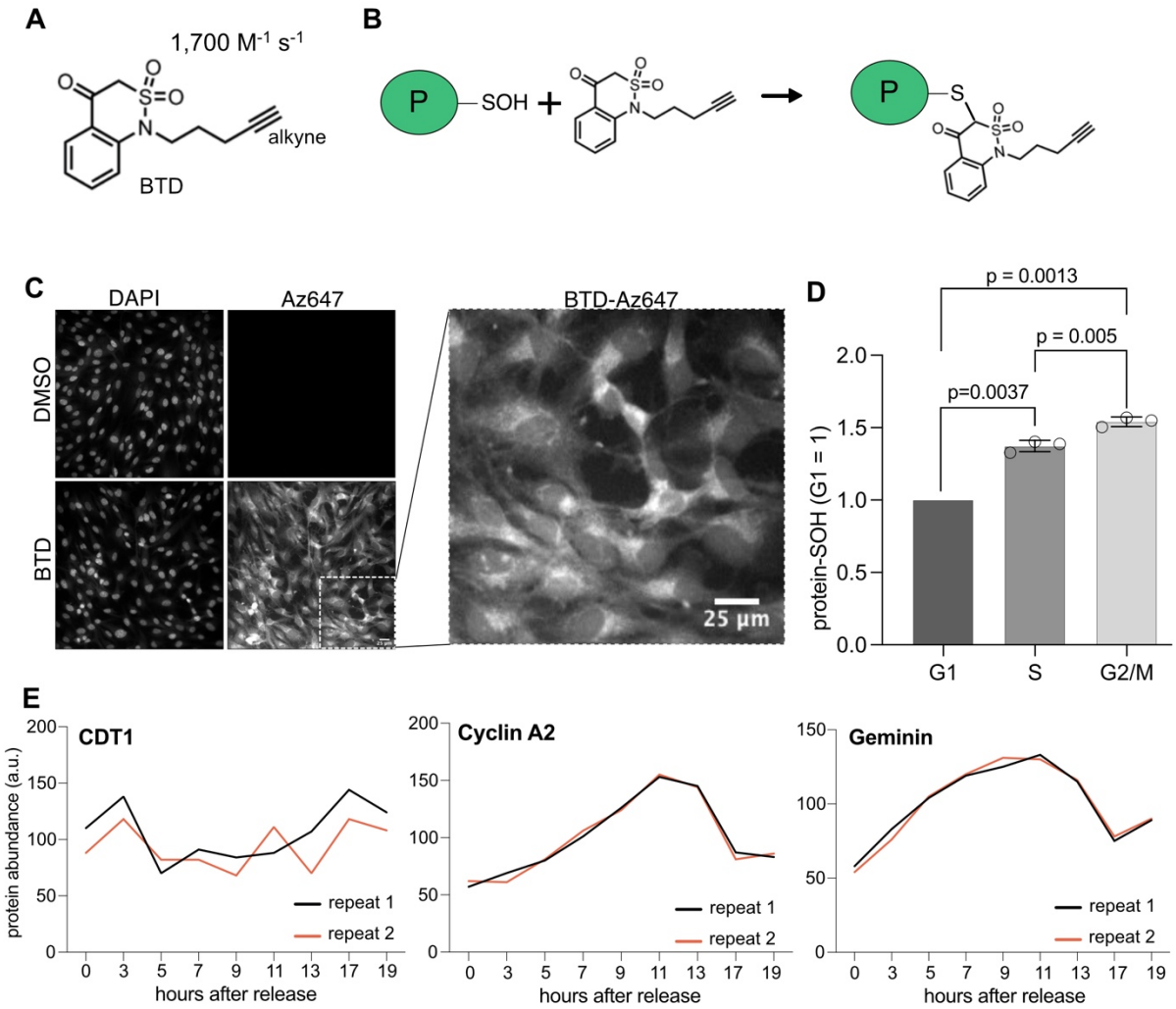

Figure S1 related to Figure 1. BTD Labeling Detects Increased S-Sulfenylation During Cell Cycle Progression

(**A**) Chemical structure and reaction rate of the sulfenic acid-specific probe BTD, containing an alkyne group for downstream click-chemistry applications[13].

(**B**) Reaction of BTD with a sulfenic acid (SOH) in living cells. P represents protein.

(**C**) *In situ* sulfenic acid staining of BTD and control (DMSO) RPE-1 cells using Azide-dye 647 (Az647) clicked to the alkyne moiety of BTD. DNA stained by DAPI. Scale bar = 25 µm, n=3.

(**D**) Flow cytometry analysis of cells treated with BTD for 1 hour, followed by fixation and visualization of sulfenic acids using Az647. The graph indicates the mean ± SD azide-fluorophore intensity relative to G1 cells. Statistical significance determined by one-sample (G1 versus S, G2/M) and paired t-test (S versus G2/M), n=3.

(**E**) Relative changes in protein abundance of known cell cycle proteins show a high degree of synchronicity in the two biological repeats (Figure 1). Protein abundance was determined by the quantitative proteomics used for normalization of the BTD cell cycle proteome. Profiles for all proteins identified are presented in Table S1.

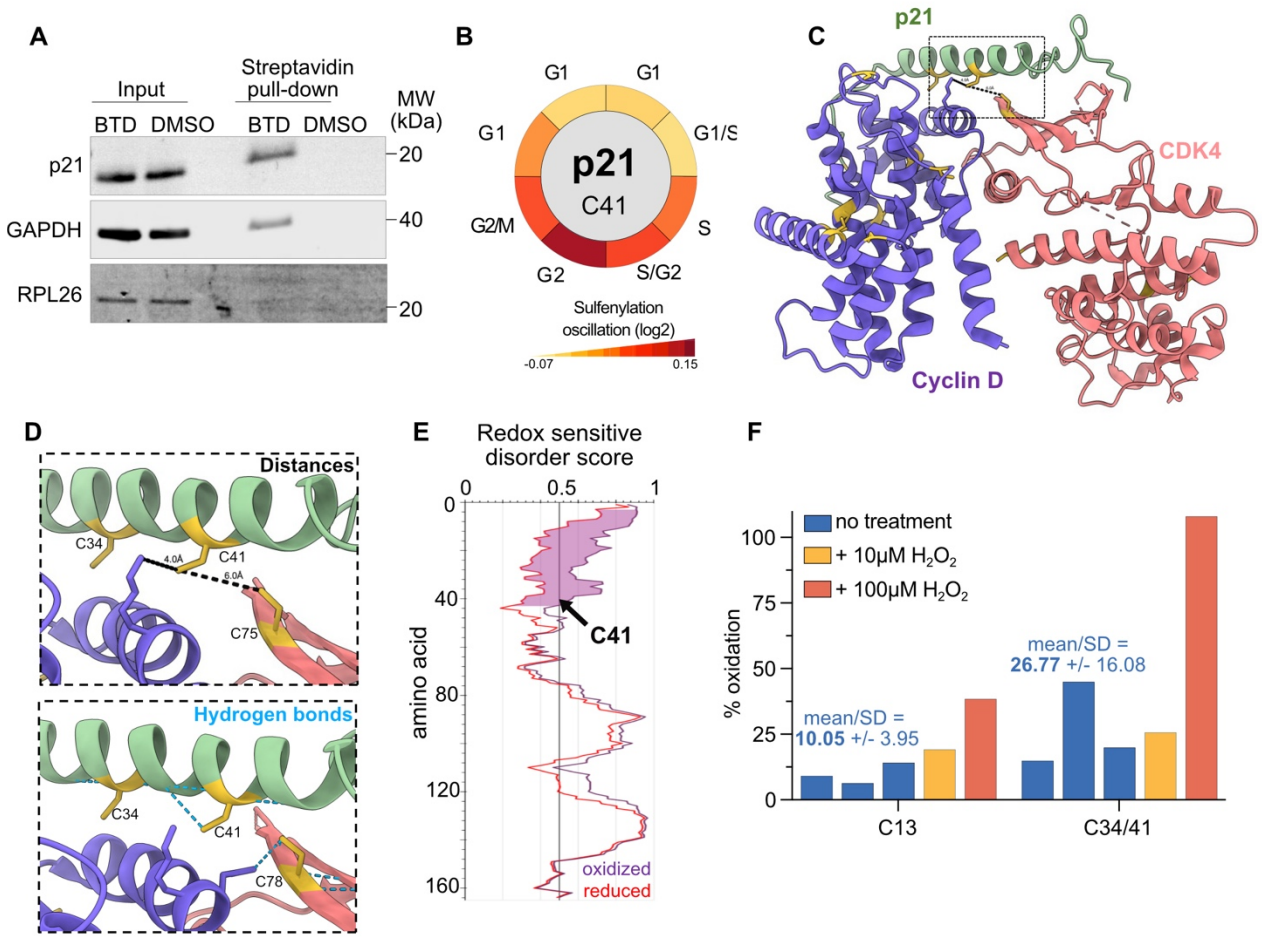

Figure 2. p21 is Oxidized on C41 During G2 Phase

(**A**) Western blot analysis confirming p21 oxidation. Click-chemistry with biotin-Dde-azide in extracts from asynchronous BTD- or Ctrl (DMSO) cells, followed by enrichment of labeled proteins on streptavidin beads, SDS-PAGE and Western blot. (n=2).

(**B**) Quantification of p21 oxidation across the cell cycle derived from quantitative mass spectrometry with the sulfenic acid-specific probe BTD.

(**C**) Structure of p21-CDK4-cyclin D (PDB: 6p8h[34]) with p21 in green, CDK4 in red, and Cyclin D in purple.

(**D**) Magnified view of the region containing C41 as indicated in (C). Relative position of p21-C41, Cyclin D, and CDK4. Top: distances, bottom: hydrogen bonds.

(**E**) IUPred3 Redox state prediction for p21. Regions with a score >0.5 are considered disordered. The prediction for p21, shown with reduced (red) or oxidized cysteines (purple) highlights a region in dark purple (AA: 3-42). Differences between both predictions indicate potential order-to-disorder changes upon oxidation[37].

(**F**) Stoichiometry of p21 cysteine oxidation determined by quantitative mass spectrometry from a biological triplicate of cells in G2 phase as illustrated in Figure S2D. H_2O_2 was added to parallel samples to fully oxidize p21 as a reference. Note, C34 and C41 reside on the same peptide and cannot be deconvolved with this approach. n=3

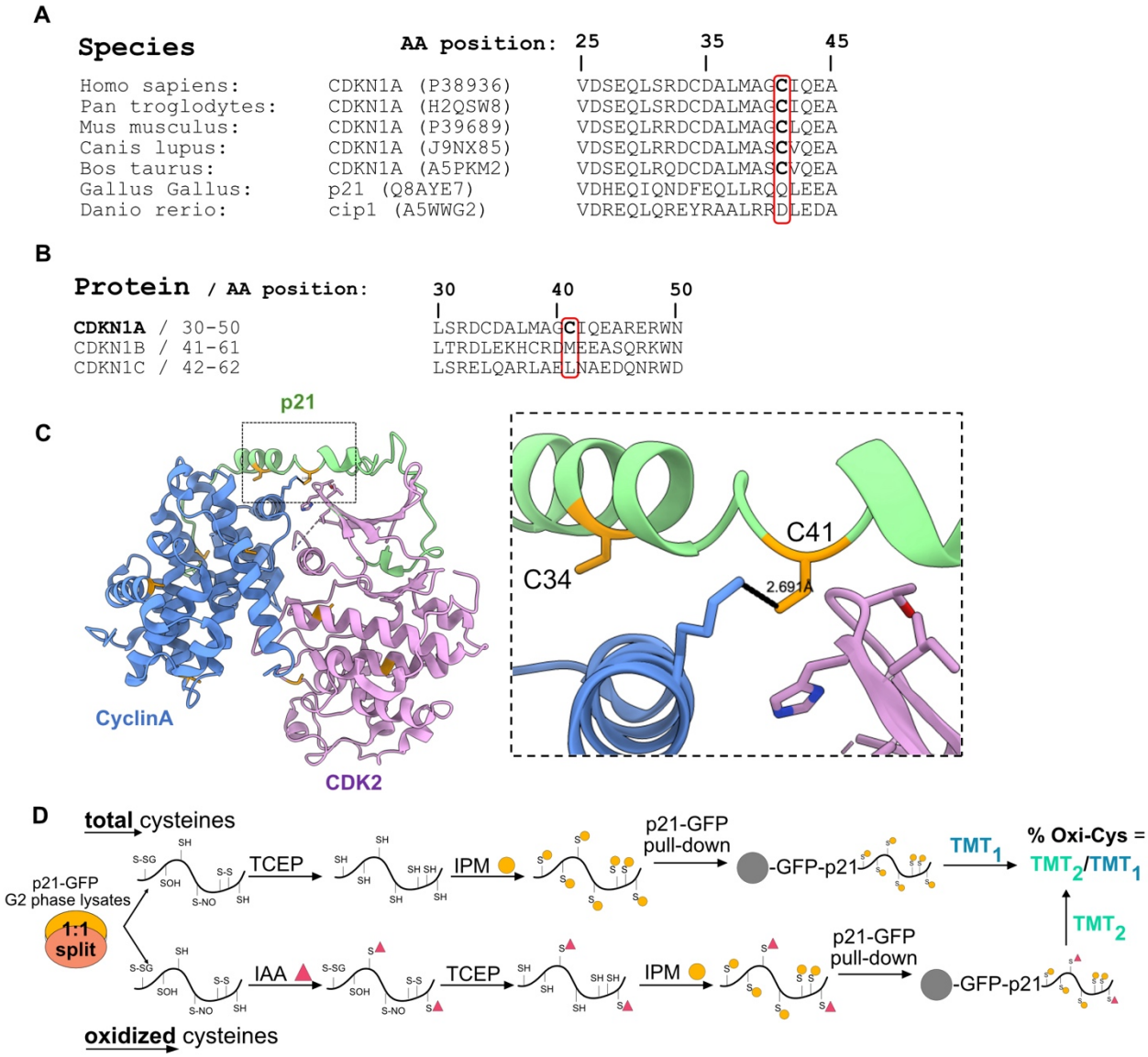

Figure S2 related to Figure 2: Conservation and Positioning of C41 in the p21-CDK2-Cyclin A Complex.

(**A**) Sequence alignment of CDKN1A (p21) highlighting conservation of C41 across vertebrates determined by ProViz[79].

(**B**) Clustal Omega alignment of CIP/KIP family members in *H. sapiens,* showing that C41 is unique to CDKN1A.

(**C**) Homology model of p21-CDK2-Cyclin A (adapted from[35]) with p21 in green, Cyclin A in blue, and CDK2 in rose. The inset illustrates the position of C41 of p21 in relation to Cyclin A and CDK2, with distances indicated.

--continued on next page--

Figure S2 related to Figure 2: Conservation and Positioning of C41 in the p21-CDK2-Cyclin A Complex. - *continued*

(**D**) Workflow to determine p21 oxidation stoichiometry. RPE-1 p21-GFP cells synchronized in G2 phase were split into two samples to collect total cysteine (top) and oxidized cysteine (bottom) samples. Total cysteines: Protein extracts were reduced (TCEP) and alkylated (IPM). Oxidized cysteines: Sample were first alkylated (IAA) to block reduced cysteines, oxidized cysteines reduced (TCEP), and alkylated (IPM). For both samples p21-GFP was enriched on GFP-binder beads, digested into peptides, TMT labelled, and samples mixed. MS analysis identified IPM-labelled cysteines and the ratio between TMT labels was used to determine the stoichiometry of oxidation.

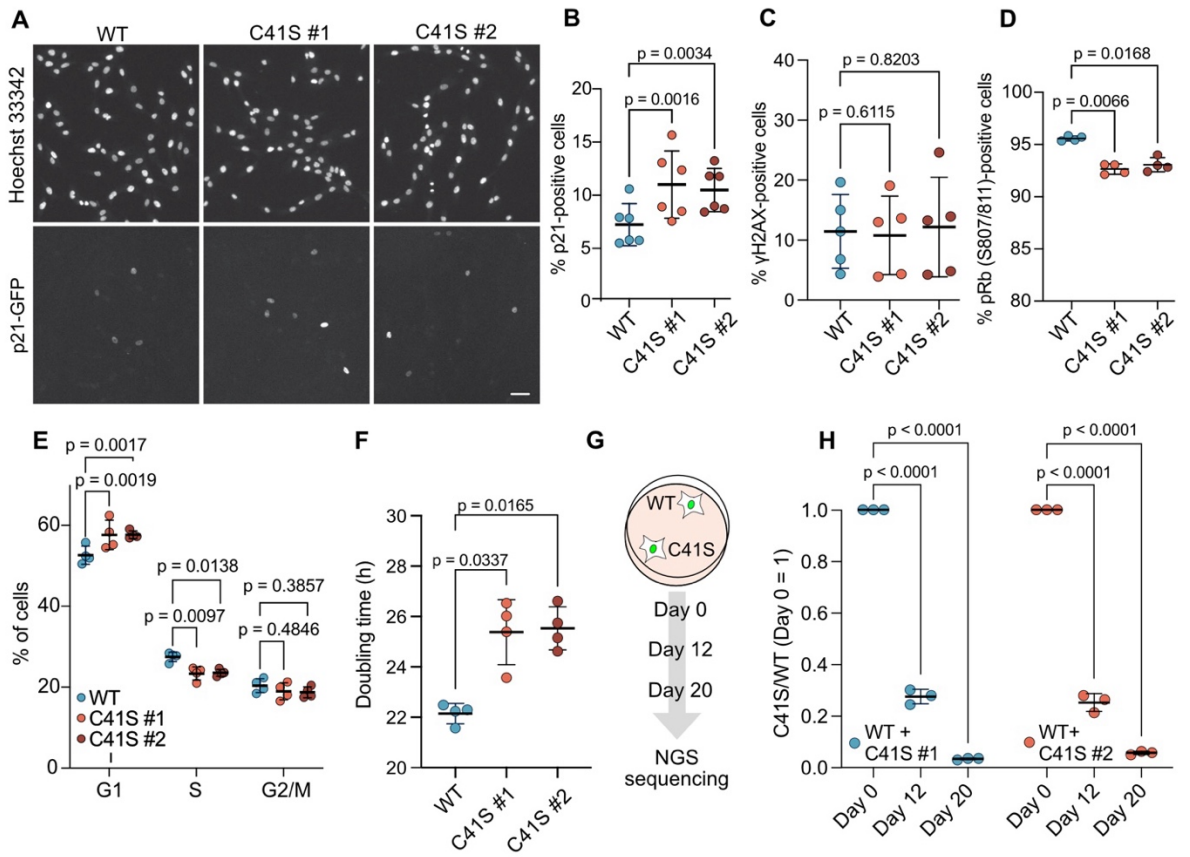

Figure 3. Mutating C41 Increases p21 Protein Levels and Impairs Proliferation

(**A**) Fluorescence microscopy showing p21-GFP-expressing WT and C41S clones #1 and #2. Nuclear staining by Hoechst 33342. Scale bar = 50 µm.

(**B**) Quantification of (A) showing the mean ± SD percentage of p21-positive cells. Statistical significance determined by one-way ANOVA, n=6.

(**C**) Quantification of γH2AX-positive WT and C41S cells. Scatter plots indicate the mean ± SD. Significance according to one-way ANOVA, n=5. Representative images are shown in Figure S3D.

(**D**) Quantification of phospho-Rb (pRb S807/811)-positive cells. Scatter plots indicate the mean ± SD. Significance determined by one-way ANOVA, n=4.

(**E**) Cell cycle distribution of WT and C41S cells determined by Hoechst 33342 staining. Plots represent the mean ± SD percentage of cells in each phase. Significance determined by two-way ANOVA, n=4.

(**F**) Doubling time in WT and C41S cells. Scatter plots indicate the mean ± SD. Significance determined by one-way ANOVA, n=2, N=4.

(**G**) Illustration of competitive growth assay between WT and C41S cells. NGS was used to determine the C41S to WT ratio at days 0, 12, and 20 of co-culture.

(**H**) Competitive growth assay between WT and C41S cells showing that C41S cells are progressively outcompeted by p21 WT cells. Data normalized to initial ratio at day 0. Scatter plots indicate the mean ± SD. Significance determined by two-way ANOVA, n=3.

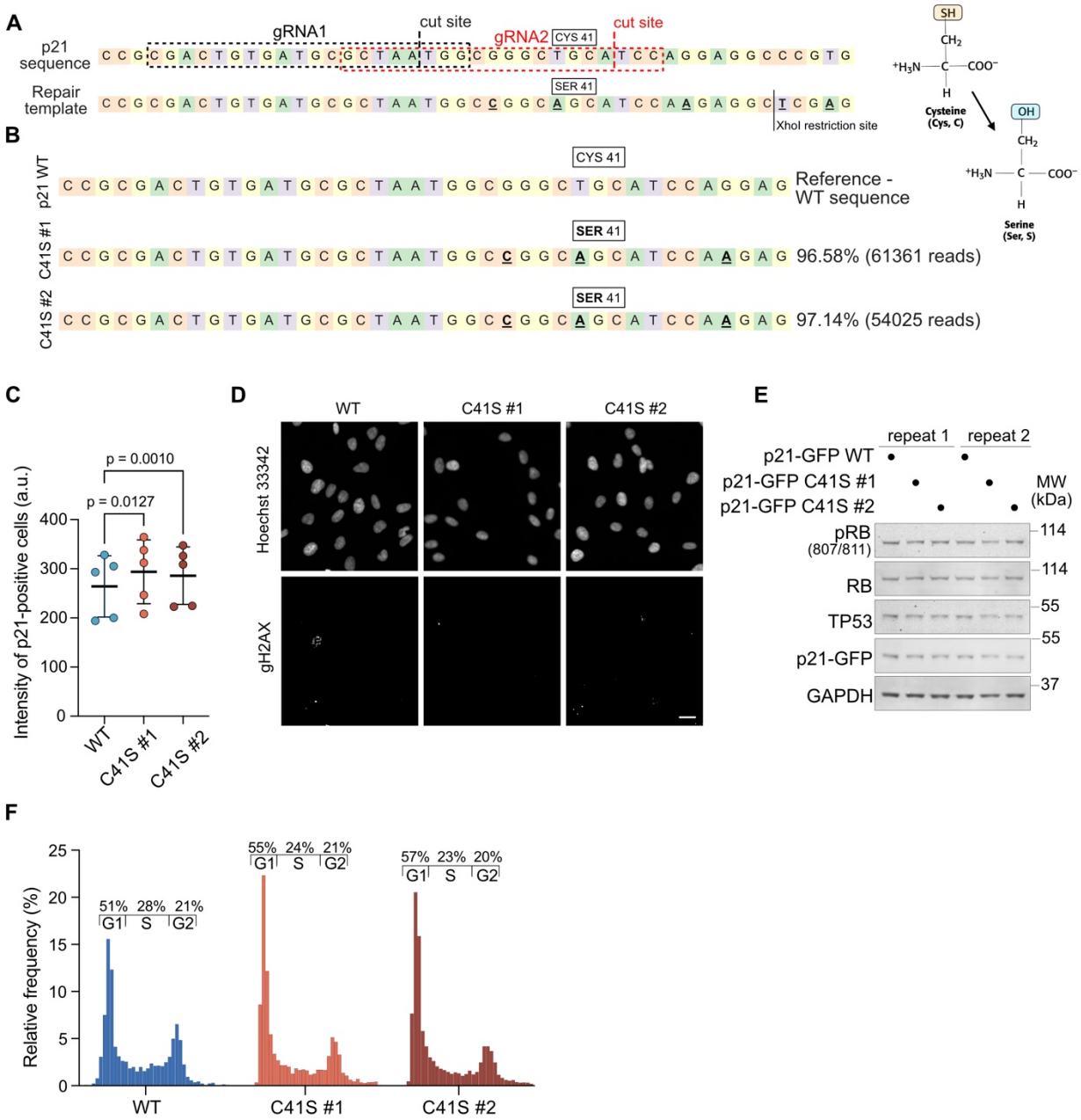

Figure S3, related to Figure3: Verification of C41S Mutagenesis and Characterization of p21-GFP WT and C41S clones

(**A**) Top: DNA sequence of p21, depicting the guide RNAs (gRNAs) used for mutagenesis. Cut sites are indicated in dashed black (gRNA1) and dashed red (gRNA2). Structure of cysteine and serine shown as reference[80].

Bottom: Sequence of the repair template replacing cysteine 41 (CYS 41) with serine (SER 41). Additional silent mutations introduced by the repair template for genotyping and digest by XhoI are indicated (bold, underlined).

--continued on next page--

Figure S3, related to Figure3: Verification of C41S Mutagenesis and Characterization of p21-GFP WT and C41S clones – *continued*

(**B**) DNA sequences of p21 WT and two C41S knock-in clones as determined by NGS. Top: p21 WT DNA flanking CYS 41. Bottom: NGS results showing prominent alleles and their frequencies for C41S #1 and C41S #2 clones. Mutated bases are underlined and indicated in bold. Minimum average read quality of 30 (1/1000 probability of an incorrect base call) was used for analysis. Only alleles with >400 reads are shown.

(**C**) Mean ± SD GFP intensity from p21-positive cells as presented in Figure 3A and 3B. Statistical significance according to one-way ANOVA, n=5.

(**D**) Immunofluorescence of WT and C41S cells showing γH2AX staining. DNA stained with Hoechst 33342. Scale bar = 50 μm. Quantification is shown in Figure 3C.

(**E**) Western blot using indicated antibodies of total lysates from asynchronous WT and C41S cells. n=2.

(**F**) Frequency distribution of integrated Hoechst 33342 intensities from equal numbers of WT and C41S cells to generate cell cycle profiles[48]. n=4.

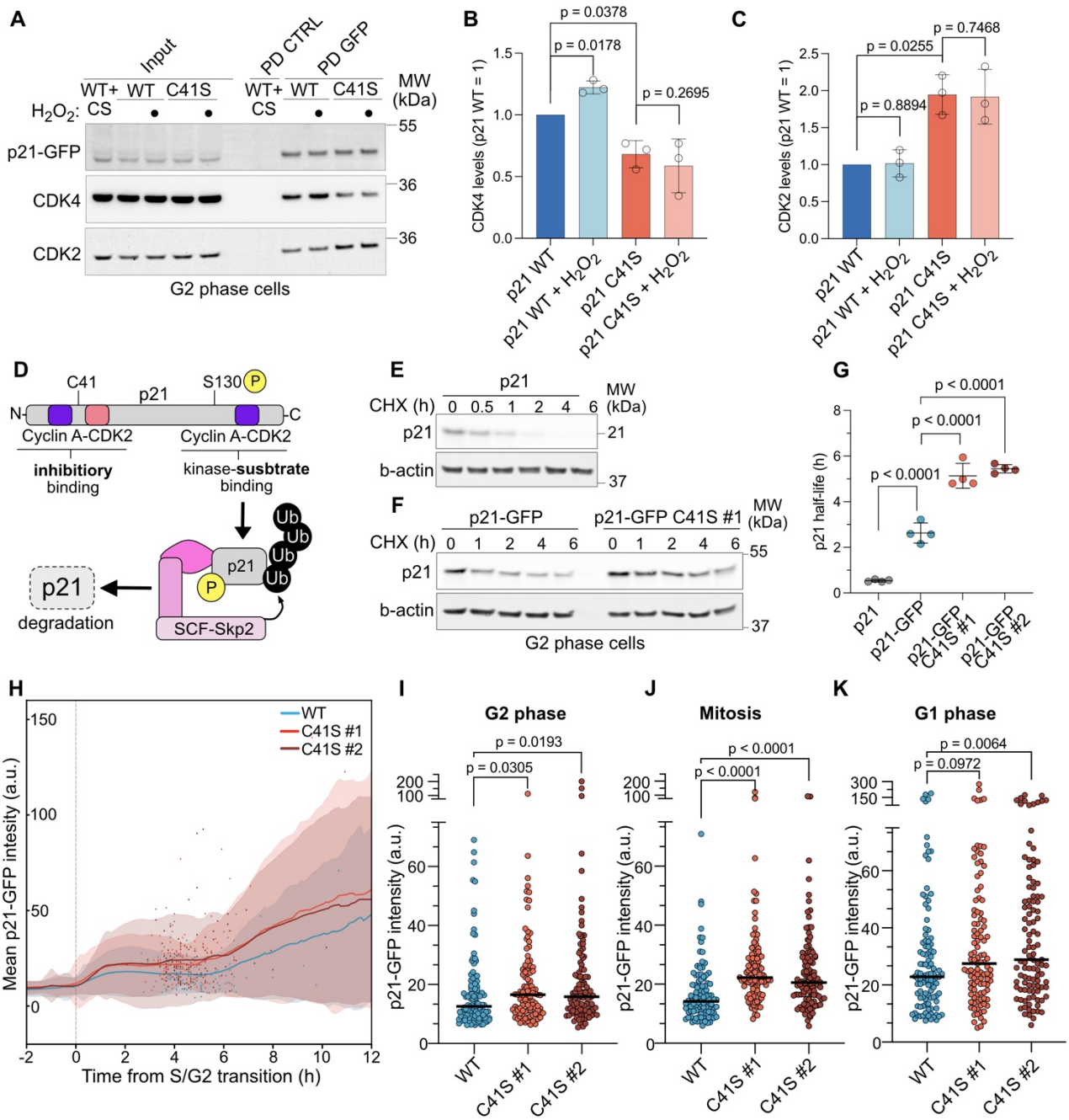

Figure 4. p21 Stability and Inheritance is Regulated by Oxidation of C41

(**A**) Western blot of p21-GFP pull-downs from G2 phase-synchronized cells showing p21 WT and C41S binding to CDK4 and CDK2 in the presence or absence of 10μM H_2O_2 that was added to living cells 30 minutes before extract preparation. Control beads lack GFP binder.

(**B, C**) Quantification of CDK4 (B) and CDK2 (C) bound to p21-GFP WT or C41S from data in (A). Bars show mean ± SD, n=3. Significance by one-sample (p21 WT vs. p21 WT+H_2O_2, p21 WT vs. p21 C41S) and paired t-tests (p21 C41S vs. p21 C41S+H_2O_2).

--continued on next page--

Figure 4. p21 Stability and Inheritance is Regulated by Oxidation of C41 - *continued*

(**D**) Illustration of p21 interactions with CDK2-cyclin A. The CDK-cyclin A complex can either be inhibited by p21 (inhibitory binding) or mediate p21 degradation (kinase-substrate binding) by SCF-SKP2 during G2 phase via S130 phosphorylation followed by ubiquitinylation and proteasomal degradation.

(**E**) Decay of untagged endogenous p21 in G2 phase cells after blocking translation with 50µg/ml cycloheximide (CHX) for the indicated time. β-actin is used as loading control.

(**F**) Comparison between the decay of C-terminally GFP-tagged p21 WT and C41S #1 after blocking translation with 50 µg/ml CHX for the indicated time.

(**G**) Half-life of p21, p21-GFP, and p21-GFP C41S #1 and #2, as determined from data shown in (E-F). Data are presented as mean ± SD, Significance by one-way ANOVA. n=3, N=4. Note, the curves used to calculate half-lives are presented in Figure S4K.

(**H**) Averaged tracks from Figure S4N, showing the dynamics of mean ± SD p21-GFP intensity from single cells expressing p21-GFP or p21-GFP C41S, computationally aligned at the S/G2 transition and followed to daughter cells in G1 phase. n=1. N=121. Dots indicate mitosis.

(**I-K**) Scatter plots of p21-GFP intensities during G2 phase (I), mitosis (J), and G1 phase (K) from the WT and C41S cells presented in (H). Black line represents mean p21-intensity. Significance according to Kruskal-Wallis with Dunn's correction. n=1, N=105.

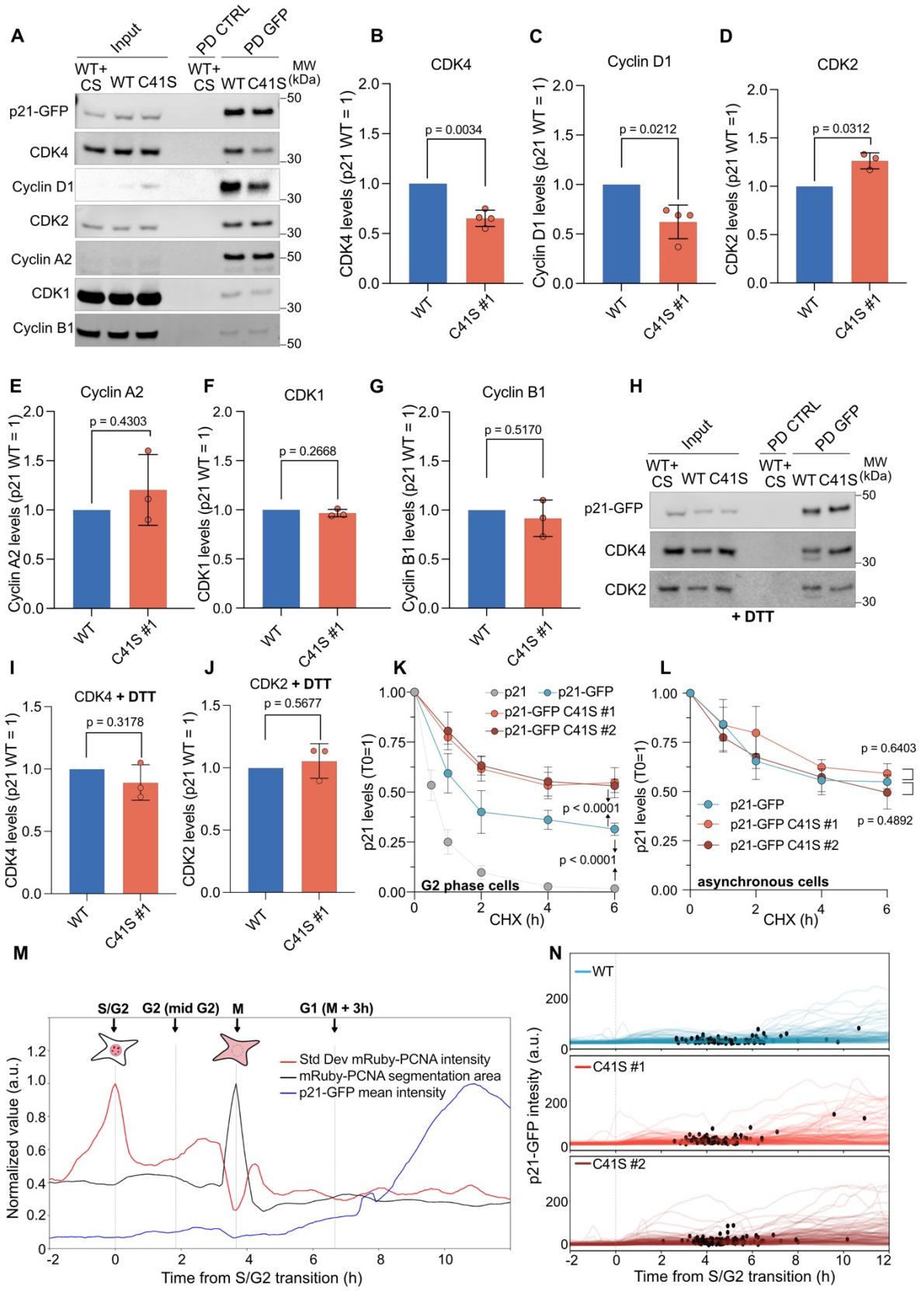

Figure S4, related to Figure 4: p21 C41S Binding to Cyclin-CDK Complexes, p21 Degradation, and Semi-automated Image Analysis of p21-GFP Levels During the Cell Cycle. ***–continued on next page--***

Figure S4, related to Figure 4: p21 C41S Binding to Cyclin-CDK Complexes, p21 Degradation, and Semi-automated Image Analysis of p21-GFP Levels During the Cell Cycle. - *continued*

(**A**) Western blot of p21-GFP pull-down experiments showing the interaction of p21-GFP, with CDK4, cyclin D1, CDK2, cyclin A2, CDK1, and cyclin B1. Control beads without GFP binder (PD CTRL).

(**B-G**) Quantification of data shown in (A) normalized to p21-WT for CDK4 (B), cyclin D1 (C), CDK2 (D), cyclin A2 (E), CDK1 (F), and cyclin B1 (G). Bars represent mean ± SD, n=4 (B-C) or n=3 (D-G). Significance by one-sample t-test.

(**H**) Western blot detecting the interaction of p21 with CDK4 and CDK2 from p21-GFP pull-downs as in (A). Here 10mM DTT was added to the extract. Control beads lack GFP binder (PD CTRL).

(**I, J**) Quantification of data shown in (H) normalized to p21-WT for CDK4 (I) and CDK2 (J). Bars represent mean ± SD, n=3. Significance by one-sample t-test.

(**K**) Quantification of data as shown in Figures 4E and 4F. Data are presented as mean ± SD, significance at time point 6h by one-way ANOVA. n=3, N=4.

(**L**) Quantification of data as shown in Figure 4F but from asynchronous cells. Data are presented as mean ± SD, significance at time point 6h by one-way ANOVA. n=3, N=4.

(**M**) Example of our semi-automated image analysis pipeline illustrating features for tracking, cell cycle classification, and fluorescence measurements from time-lapse imaging of RPE-1 cells expressing p21-GFP and mRuby-PCNA. Cells were tracked using a merged mask obtained from nuclear mRuby-PCNA and p21-GFP intensities. The S phase is characterized by bright replication foci, thus the S/G2 transition can be identified using the peak in standard deviation of mRuby-PCNA. Mitosis is characterized by an increase in the segmentation area due to the distribution of PCNA in the whole cytosol of mitotic cells, after nuclear envelope breakdown. p21-GFP levels were measured throughout the time-lapse or at defined time points for mid G2 phase, mitosis (M), and G1 phase as indicated in the panel.

(**N**) Single cell tracks from time-lapse imaging of p21-GFP, p21-GFP C41S #1, and p21-GFP C41S #2 cells aligned at S/G2 phase transition. Mitoses indicated by black dots. n=1, N=121.

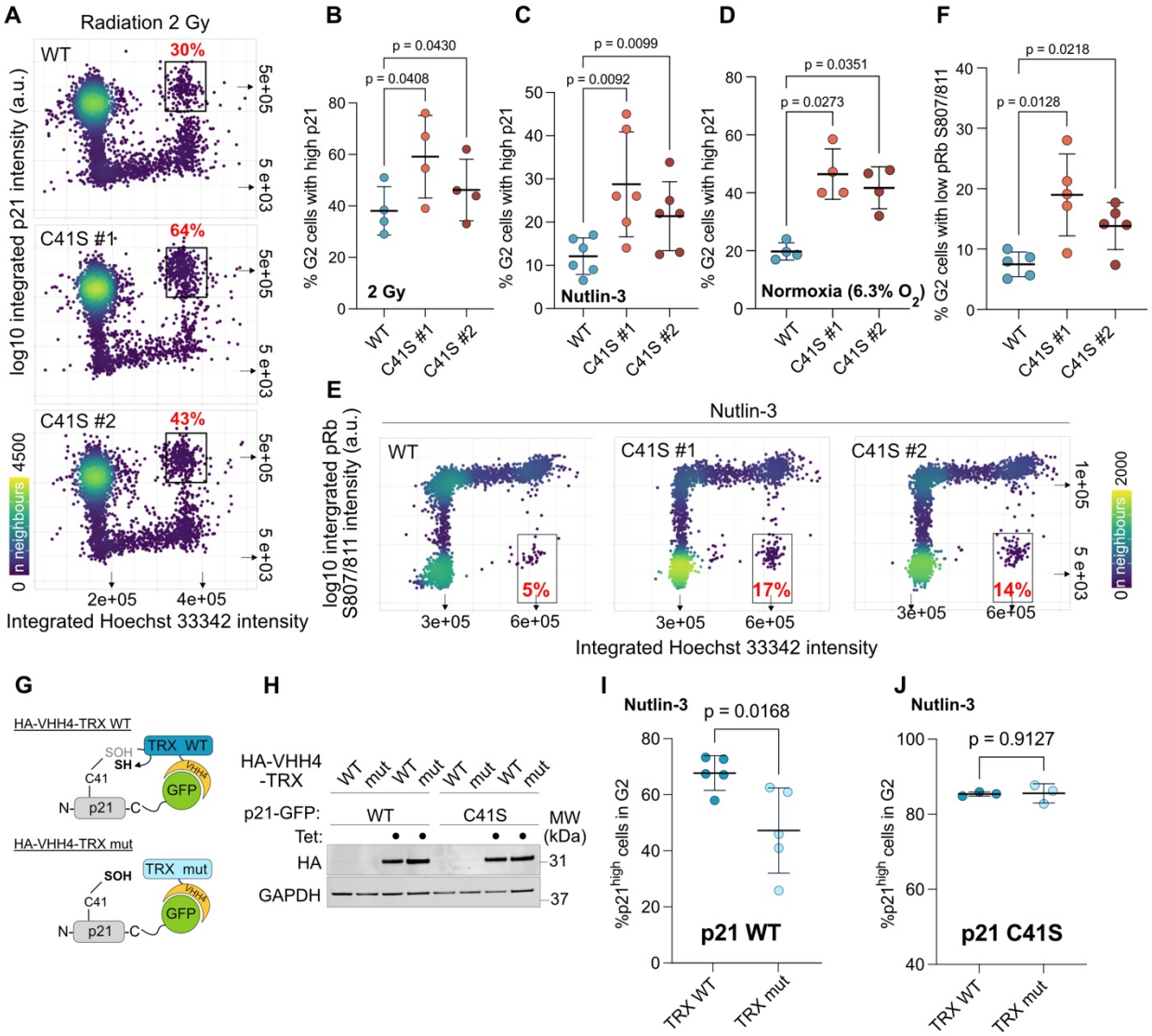

Figure 5. The Redox State of C41 Determines Sensitivity to DNA Damage and p53 Signaling

(**A**) Bivariate density plots depicting p21 levels and DNA content (Hoechst 33342) in WT and C41S cells, 24 hours post 2Gy irradiation. Numbers in red refer to the percentage of G2 cells that express high levels of p21, as indicated by the black box. Corresponding untreated cells are shown in Figure S5A.

(**B**) Quantification of data from (A) showing the mean ± SD percentage of G2 cells with high p21 expression 24 hours post 2Gy irradiation. Significance according to one-way ANOVA, n=4.

(**C**) Mean ± SD percentage of G2 cells with high p21 expression after 24 hours of treatment with 1μM nutlin-3 to activate p53 signaling. Significance according to one-way ANOVA, n=6.

---continued on next page---

Figure 5. The Redox State of C41 Determines Sensitivity to DNA Damage and p53 Signaling -*continued*

(**D**) Mean ± SD percentage of G2 cells with high p21 expression after nine to eleven days of normoxic cell culture (6.3% O_2 for RPE-1 cells, [56,57]), which induces DNA damage and p21 (see Figure S5B-E), Significance according to one-way ANOVA, n=3, N=4.

(**E**) Bivariate density plots showing phospho-Rb (pRb S807/811) levels in G2 phase in WT and C41S cells after 24 hours of nutlin-3 treatment (1µM). Percentage of G2 cells with low pRb (S807/811) expression is indicated in the black box. Corresponding untreated cells are shown in Figure S5F.

(**F**) Quantification of data from (E) representing the mean ± SD. Statistical significance determined by one-way ANOVA, n=5.

(**G**) Illustration of experimental setup controlling the redox state of p21-GFP C41 in living cells. Tetracycline-inducible expression of an GFP-nanobody fused to wildtype (WT) antioxidant enzyme Thioredoxin (TRX) maintains p21-GFP C41 in a reduced state, mimicking the effect of C41S. The Inactive TRX mutant (HA-VHH4-TRX mut) serves as negative control.

(**H**) Western blot analysis showing the tetracycline-induced expression of the HA-VHH4-TRX WT and HA-VHH4-TRX mut constructs used for the experiments shown in (I,J).

(**I**) Scatterplot showing the mean percentage ± SD of G2 cells with high p21 expression for p21-GFP WT cells expressing tetracycline-induced HA-VHH4-TRX WT or HA-VHH4-TRX mut. Cells were treated with 1µM nutlin-3 for 24 hours. Corresponding bivariate density plots used for gating are presented in Figure S5G. Statistical significance determined by paired t-test, n=5.

(**J**) Scatterplot showing the mean percentage ± SD of G2 cells with high p21 expression for p21-GFP C41S cells expressing tetracycline-induced HA-VHH4-TRX WT or HA-VHH4-TRX mut. Cells were treated with 1µM nutlin-3 for 24 hours. Corresponding bivariate density plots used for gating are presented in Figure S5H. Statistical significance determined by paired t-test, n=3.

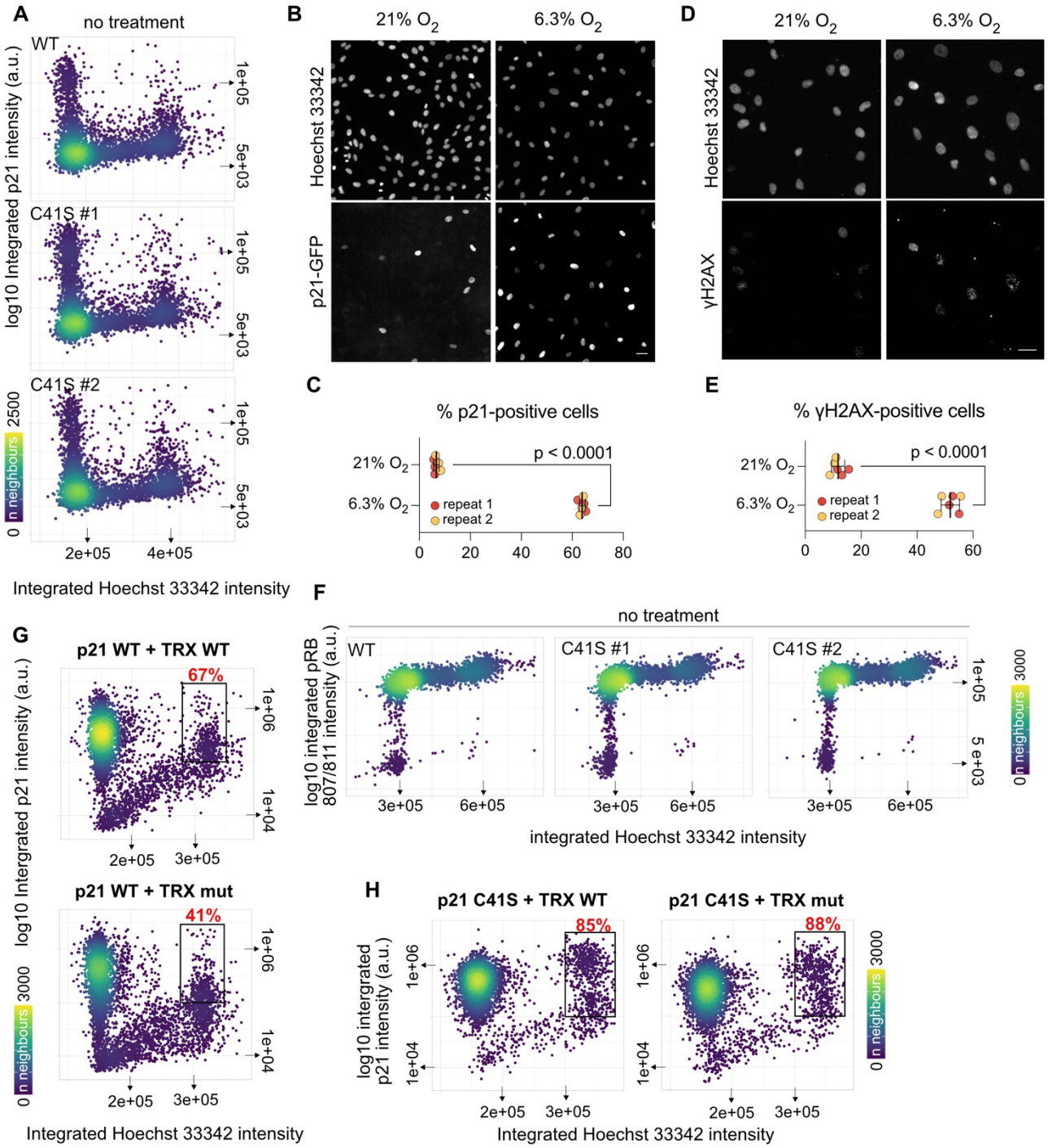

Figure S5 related to Figure 5: Normoxic Cell Culture Induces DNA Damage and Response of p21-GFP to Localized TRX Expression.

---continued on next page---

Figure S5 related to Figure 5: Normoxic Cell Culture Induces DNA Damage and Response of p21-GFP to Localized TRX Expression. – *continued*

(**A**) Bivariate density plots showing DNA content (Hoechst 33342) and p21 levels in WT and C41S cells in unperturbed conditions. Related to Figure 5A.

(**B**) Fluorescence microscopy images showing p21-GFP and Hoechst 33342 staining in RPE-1 cells expressing endogenous p21-GFP, cultured at 21% O_2 (hyperoxia) or 6.3% O_2 (normoxia). Scale bar = 50 µm.

(**C**) Quantification of data shown in (B), showing increased p21 levels upon cell culture at 6.3% O_2. Data represent mean ± SD percentage of p21 positive cells. Significance assessed by paired t-test, n=2, N=6. Note: due to the experimental setup, cells cultured at different O_2 concentrations were seeded on separate imaging plates. To ensure the highest comparability, IF staining was performed in parallel with the same reagents and imaging settings and analysis settings were identical for plates cultured in 6.3% and 21% O_2.

(**D**) Immunofluorescence images of p21-GFP WT cells stained for γH2AX and Hoechst 33342 after culturing at 21% O_2 or 6.3% O_2. Scale bar = 50 µm.

(**E**) Quantification of data shown in (D). Statistical significance assessed by paired t-test, n=2, N=6.

(**F**) Bivariate density plots showing Hoechst 33342 and pRb S807/811 staining in WT and C41S cells in unperturbed conditions. Related to Figure 5E.

(**G**) Bivariate density plots showing Hoechst 33342 and p21-GFP intensities in p21-GFP WT cells expressing tetracycline-induced HA-VHH4-TRX WT or HA-VHH4-TRX mut, after 24 hours of treatment with 1µM nutlin-3. Corresponding quantification is presented in Figure 5I. Percentage of G2 cells that express high levels of p21 is indicated by the black box.

(**H**) Bivariate density plots showing Hoechst 33342 and p21-GFP intensities in p21-GFP C41S cells expressing tetracycline-induced HA-VHH4-TRX WT or HA-VHH4-TRX mut, after 24 hours of treatment with 1µM nutlin-3. Corresponding quantification is presented in Figure 5J. Percentage of G2 cells that express high levels of p21 is indicated by the black box.

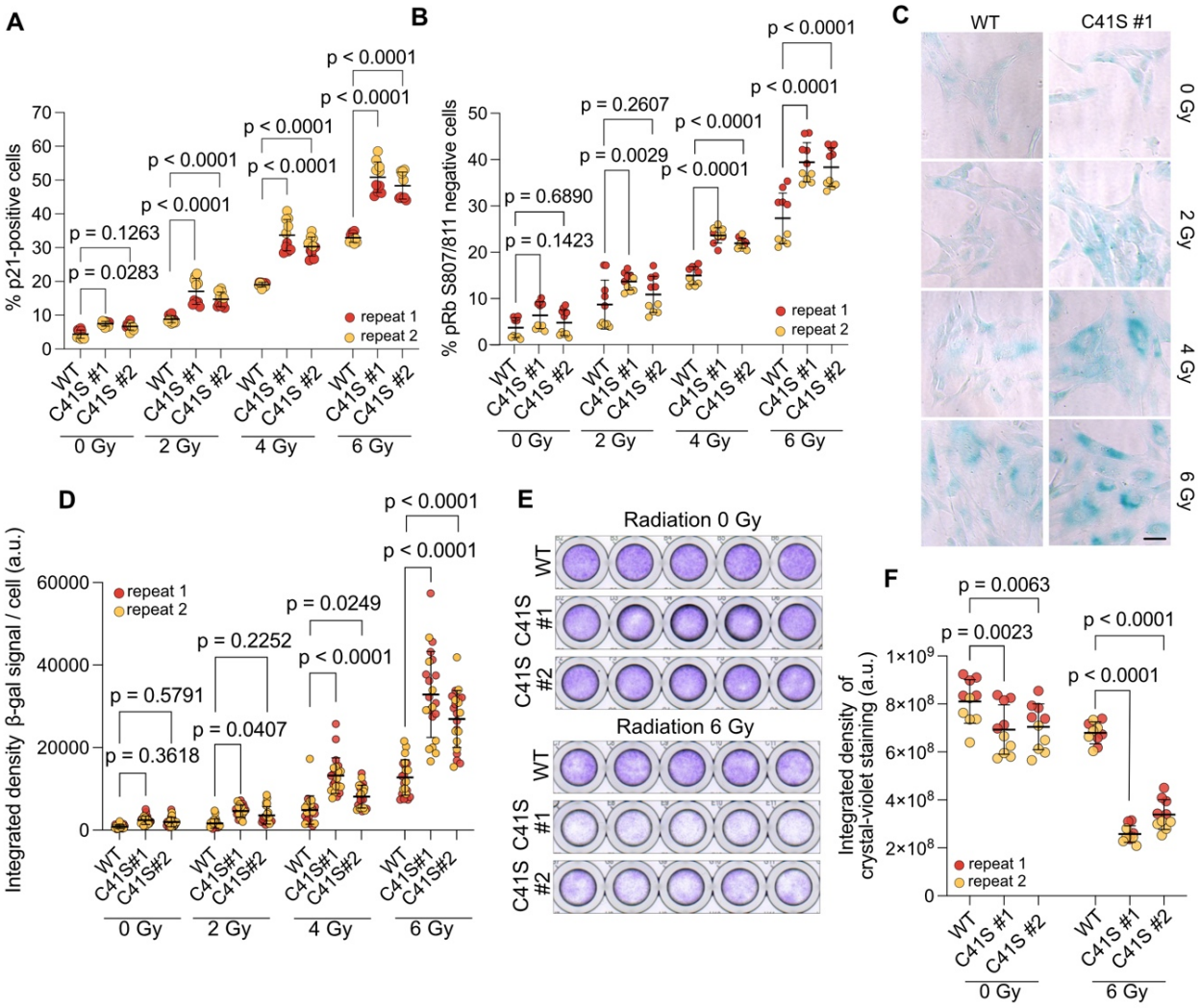

Figure 6. Non-Oxidizable C41 Primes Cells for Cell Cycle Exit into Senescence.

(**A, B**) Scatter plots showing the mean ± SD percentage of p21-GFP-positive (A) and pRb S807/811-negative (B) WT and C41S cells, as determined by fluorescence imaging (A) or immunostaining (B) six days after treatment with the indicated dose. Statistical significance determined by two-way ANOVA, n=2, N=10.

(**C**) Representative images showing β-galactosidase staining six days after irradiating WT or C41S cells with the indicated doses of Gy. Scale bar = 50 µm.

(**D**) Scatter plot showing the quantification of β-galactosidase staining in response to irradiation in WT and C41S cells from the experiment shown in (C). Data represent the mean ± SD β-galactosidase staining (integrated density) per cell. Statistical significance determined by two-way ANOVA, n=2, N=22.

(**E**) Crystal-violet staining showing reduced proliferation in C41S compared to WT cells in unperturbed conditions and ten days after irradiation with 6Gy.

(**F**) Quantification of data in (E), showing the mean ± SD intensity of crystal-violet staining. Significance according to two-way ANOVA, n=2, N=10.

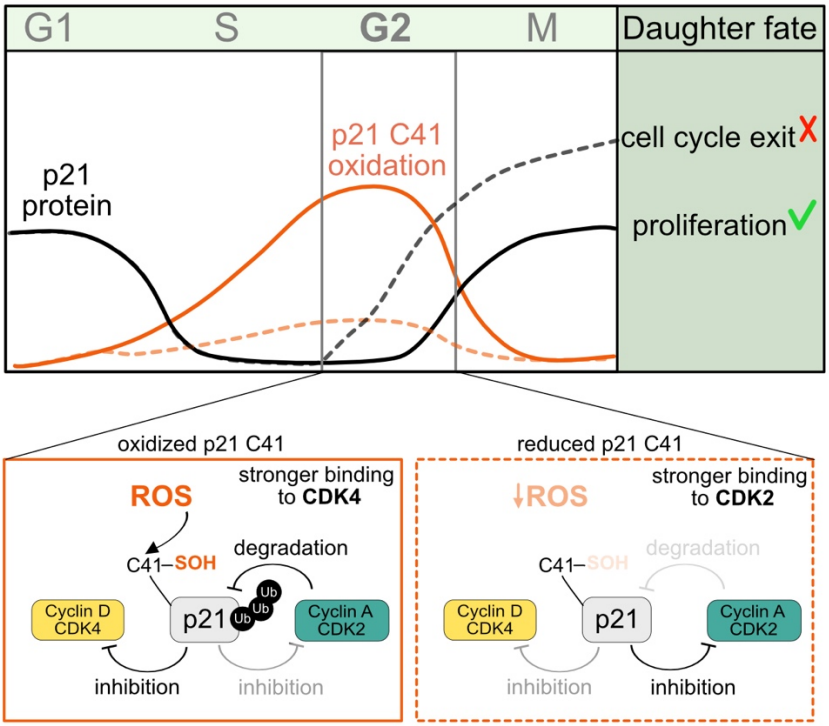

Figure 7. Model of a Redox-Regulated Negative Feedback Between p21 and CDK2.

Model illustrating how C41 oxidation controls the proliferation-senescence decision by modulating the feedback between p21 and CDKs.

Top: p21 protein (black) and C41 oxidation (orange) levels across the cell cycle. Oxidation of p21 C41 peaks in G2 phase. Decreased p21 oxidation (dashed orange) results in impaired p21 degradation in G2 and therefore in increased p21 protein levels (dashed black). Excessive p21 levels are inherited by daughter cells, where p21 promotes cell cycle exit into quiescence or senescence.

Bottom left: oxidized C41 allows preferential binding of the p21 N terminus to CDK4-cyclin D in G2 phase cells and enables recruitment of CDK2-Cyclin A to the C-terminal cyclin motif of p21, thereby targeting p21 for proteasomal degradation via the SCF-SKP2 ubiquitin ligase.

Bottom right: Decreased oxidation of C41 directs binding of the p21 N terminus to CDK2-Cyclin A instead of CDK4-Cyclin D inhibiting CDK2 and thus reducing p21 degradation and leading to p21 accumulation and subsequent cell cycle exit.

EXPERIMENTAL PROCEDURES

Cell lines are listed in Table S2, gRNAs and ssODNs in Table S3, plasmids in Table S4, PCR primers in Table S5, and antibodies in Table S6. All key resources and key equipment used in this study are listed in Table S7 unless specified directly in the text.

Cell culture and cell lines

All cell lines were cultured according to standard mammalian tissue culture protocol at 37°C in 5% CO_2 and at 21% or 6.3% O_2 as indicated in the Figures and tested for mycoplasma contamination. The parental cell line hTERT RPE-1 FRT/TR used for Mass Spectrometry analyses (RRID:CVCL_VP32) was kindly provided by Jonathon Pines (ICR, London, UK). hTERT RPE-1 FRT/TR mRuby-PCNA + p21-GFP cells used for p21 experiments (RPE-1 p21-GFP) were kindly provided by Alexis Barr (Imperial College London, UK). RPE-1 Cells were grown in DMEM/F12 supplemented with 10% (v/v) FBS, 1% (v/v) penicillin-streptomycin, 1% Glutamax, 0.5ug/ml Amphotericin B and 0.26% sodium bicarbonate. For experiments at 6.3% O_2, cells were adapted for five days before experiments using an InvivO 2 500 workstation (Baker Ruskinn) and concluded before day 12 of cell culture at 6.3% O_2. All liquids used were adapted for at least 2 hours in 6.3% O_2 to equilibrate to the ambient oxygen concentration. Tetracycline inducible HA-VHH4-TRX RPE-1 cell lines were created by electroporation 1-2x106 cells with in 100µl tips with plasmids PL4 and PL5, respectively, mixed with PL6 in a ratio of 1:3 using a Neon Transfection System with two pulses at 1350V and 20 ms. After 4 days cells were expanded on 15 cm dishes and selected with 500 µg/mL neomycin for 14-21 days. Single positive clones were picked and analysed by anti-HA immune-staining followed induction with 100 µg/ml tetracycline to assess uniform HA-VHH4-TRX expression. All the cell lines are listed in Table S2 and plasmids in Table S4.

Crispr/Cas9-engineering and NGS sequencing

CRISPR-Cas9 mediated gene editing was performed using ouabain-selection pioneered by[42] based on a plasmid kindly provided by Yannick Doyon (Table S4). We inserted an additional U6-gRNA cassette with BsmBI restriction sites to incorporate two different gRNAs targeting p21 (PL3). gRNAs were selected using the CRISPick webtool (BROAD Institute) (RD2, RD3). Phosphorothioated single-stranded DNA repair templates (ssODN)

for ATP1A1 [42] (RD4) and p21 (RD5) were synthesized by Integrated DNA Technologies (IDT). Sequences for gRNAs and ssODNs are listed in Table S3. To facilitate screening for positive C41S integrands an XhoI site was inserted into ssODN (RD5) at wobble positions (Figure S3A). 300.000 RPE-1 p21-GFP cells were electroporated with a Neon Transfection System using a 10µl tip and two pulses at 1350V and 20ms with 500ng p21 gRNA/Cas9 plasmid PL3 (Table S4) mixed with 2pmol of ATP1A1 ssODN (RD4) and 6pmol p21 ssODN (RD5). After 3-4 days cells were expanded into 15 cm dished and treated with 0.25µM ouabain, followed by isolation of single clones 7-12 days after drug addition and clone expansion. Genomic DNA was prepared using EZNA Tissue DNA kit according to the manufacturer's instructions and amplicons were amplified by PCR using DNA oligos listed in Table S3 for restriction (PCR1 + PCR2) and NGS analysis (PCR3-8 +PCR9). For NGS by GeneWiz (Azenta Life Science) 6 nucleotide long unique barcodes were added to analyse WT and C41S cells together. NGS sequences were analysed by CRISPResso2 [81] using a script containing the amplicon sequences, gRNA sequence, trimming parameters (TruSeq3-PE), quality threshold (set to a minimum of 30), minimum reads overlap (set to 150), and sample name:

CRISPResso --fastq_r1 1_R1_001.fastq.gz --fastq_r2 1_R2_001.fastq.gz --amplicon_seq seq1, seq2,seq3,seq4,seq5,seq6 --amplicon_name cl1,cl2,cl3,cl4,cl5,cl6, --guide_seq GCGACTGTGATGCGCTAAT --trim_sequences --trimmomatic_options_string ILLUMINACLIP:TruSeq3-PE.fa:2:30:10:2:True --min_average_read_quality 30 --max_paired_end_reads_overlap 150 -qwc 112-132 -n sample_1;

Allele frequency tables were used for determination of genotype (Figure S3) and to calculate ratios in cell competition experiments (Figure 3). Only alleles with >400 reads were considered. Related to Figures 3 and S3.

BTD

BTD to label sulfenic acids in living cells for initial tests [13,26] was kindly gifted by Kate Carroll (UF Scripps Biomedical Research, USA). BTD for mass spectrometry, flow cytometry, localization and pull-down experiments was synthesised according to [26] by André Nadler and Kirstin Bohlig (MPI-CBG, Dresden, Germany). Lyophilised BTD was dissolved in water-free 100% DMSO to a final concentration of 200mM, aliquoted and dried. For labeling of sulfenic cells BTD aliquots were re-dissolved in 100% DMSO and

vortexed thoroughly. Once dissolved in DMSO for labeling each aliquot was frozen only once to ensure probe integrity. Related to Figures 1, 2 and S1.

Cell cycle synchronization and cell treatments

For cell cycle-dependent synchronization RPE-1 cells were seeded at low density (<8000 cells/cm^2) and incubated with 150nM palbociclib for 24 hours. Afterwards, cells were washed 2-3x with warm PBS, released into fresh cell culture media and collected at indicated time points after the release. For p21-oxidation stoichiometry and half-life experiments, cells were synchronised in G2 phase by 11 hours release from palbociclib treatment. For the latter, 50µg/ml cycloheximide (CHX) was added to the cell culture media after the release for the indicated time. To induce p53 cells were treated with the indicated concentrations of nutlin-3 or irradiated with the indicate dose (Gy) on a X-ray generator with and MP1 controller (Gulmay). Related to Figures 1, 2, 4, S1 and S4.

Doubling-time Analysis

To assess the doubling time of cells, a defined number of cells were seeded into 6-well dishes and the time until the next splitting precisely noted. Before cells reached confluency (usually 3-4 days) they were trypsinised, collected in media, fixed in 4% PFA for 10 minutes, pelleted, and resuspended in PBS for cell counting using an automated cell counter (Countess, Thermo Fisher). Then the doubling was calculated according to: *Doubling Time = [T × (ln2)] / [ln (Xe / Xb)]*. With T = time, Xe = number of cells at the end, Xb= number of cells at the beginning. Related to Figure 3.

Growth-competition

p21-WT and p21-C41S (#1 or #2) cells were mixed roughly 50:50, seeded into dishes, and a sample was taken for later NGS analysis (day 0). The mixed cell population was passaged regularly before cells reached confluency and at day 12 and day 20 samples were taken for NGS analysis. For NGS genomic DNA was extracted and a short genomic region around C41 of CDK1NA (p21) was amplified using the primers indicated in Table S5. The resulting PCR product was gel-purified and sent for NGS by GeneWiz (Azenta Life Science). Different timepoint were analysed in parallel using bar coded primers as detailed above. The alleles frequency table was used to collect the precise number of

reads corresponding to the WT or C41S sequence and used to express the ratio of C41S/WT of day 12 and 20 relative to day 0. Related to Figure 3.

β -galactosidase staining

β-galactosidase staining was performed with the Senescence and β-galactosidase Staining Kit according to the manufactures instructions. In brief, p21-WT and C41S (#1 and #2) cells, treated with indicated doses of Gy, were seeded into clear 96-well plates and the next day washed 2x in PBS and fixed for 15 minutes with the provided fixative solution. Cells were washed 2x in PBS and incubated with β-galactosidase Staining Solution (adjusted to pH 5.9-6.1) ON at 37°C in a dry incubator (no CO_2). Subsequently cells were washed twice in PBS and incubated with 1µg/ml DAPI for 10 minutes to stain nuclei. Lastly, cells were washed 2x before imaged in PBS. Related to Figure 6.

BTD staining

For fluorescence microscopy analysis of BTD-labeling RPE-1 cells were seeded in microscopy slides (IBIDI), incubated with 1 mM BTD or 0.5% DMSO for one hour in serum-free cell culture media. Subsequently, cells were washed twice, fixed in 4% Paraformaldehyde (PFA)/PBS supplemented with 5mM Iodoacetamide (IAA) to block reduced thiols. Then, cells were 2x washed with PBS, permeabilized with -20°C 90% methanol for 15 minutes, washed once more in PBS and blocked in 5% BSA-PBS for 30 minutes at RT on a horizontal shaker. BTD-labelled proteins were clicked to azide-647 performing a CuAAC-click reaction. Briefly, Copper(II)-sulfate (CuSO4) was combined with Sodium Ascorbate and Tris[(1-benzyl-1H-1,2,3-triazol-4-yl)methyl]amin) (TBTA) to reach 1mM CuSO4, 0.1mM TBTA, 1mM Sodium Ascorbate, 0.1nmol azide-647. After one hour, protected from light, the click mix was removed, cells were washed 3x in PBS containing 20mM EDTA and 0.02% Tween, stained with 1ug/ml DAPI for 10 minutes and washed once more before imaging. Related to Figure S1.

Crystal-violet staining

p21-WT and C41S cells, treated with indicated doses of Gy, were seeded into clear 96-well plates and collected once p21-WT cells reached full confluency. Cells were washed 2x in PBS and fixed in ice-cold 90% methanol for 10 minutes. Methanol was removed and

cells were stained with 0.1% crystal-violet in 25% methanol for 10 minutes. Staining was removed and cells washed 4x with distilled water. Plates were dried completely and stored protected from light before imaging. Related to Figure 6.

Immunofluorescence staining

To detect pRb 807/811 and γH2AX by immunofluorescence (IF) cells were seeded into black 96-well plates, cultured for 2-3 days, washed 2x in PBS, and fixed with 4% PFA/PBS for 15 minutes at RT on a horizontal shaker. For the experiments in normoxia, cells were fixed in an InvivO 2 500 workstation (Baker Ruskinn) at 6.3% O_2 before further processing at atmospheric oxygen. After fixation, cells were washed twice in PBS, permeabilized with 0.2% Triton X-100 + 0.01% SDS in PBS for 10 minutes and blocked in 2% BSA in PBS/0.1% Triton X-100 for 30-60 minutes. Primary antibodies were added in the blocking solution and incubated for 1 hour at RT or ON at 4°C. Afterwards, cells were washed twice with PBS and incubated with the corresponding secondary antibody for 1 hour at RT, followed by 3x washes in PBS, staining of DNA with 1ug/ml Hoechst-33342 for 15 minutes. Cells were washed twice more in PBS before imaging. All primary and secondary antibodies used in this study are indicated in Table S6. Related to Figures 3, 5, 6, S1, S3 and S5.

Flow cytometry

For flow cytometry cells were trypsinised, washed once in PBS, fixed in ice-cold 70% ethanol, washed in PBS and resuspended in 50µg/ml propidium iodide (PI)-staining solution supplemented with 100µg/ml RNAse. Samples were analysed on an LSRII–analyser (BD) and 10.000 events per sample collected to create cell cycle profiles indicated in Figure 1B. For cell cycle sulfenic acids analysis, cells were labelled with BTD for 30 minutes in cell culture media containing 1% serum, then washed twice, trypsinised, and fixed with 4% PFA/PBS supplemented with 5mM IAA. Then cells were permeabilized with 90% ice-cold methanol and blocked for 30 minutes in 5% BSA-PBS. Click-reactions with 3 million cells containing 2nmol azide-488 were performed in click buffer (1mM CuSO4, 0.1mM TBTA, 1mM sodium ascorbate) for 1 hour on a rotation-wheel in the dark. Afterwards, cells were washed 3x in PBS containing 20mM EDTA, stained with 1µg/ml DAPI, washed 3x in PBS and 50.000 events were analysed on an

LSRII–analyser (BD). Data analyses were performed with FlowJo TM (Becton Dickinson & Company (BD) 2023, version: 10.9) Related to Figures 1 and S1.

SDS-Page and Western-blot

Total cell lysates were obtained by washing cells twice in PBS followed by adding 1x NuPAGE LDS Sample buffer containing 100mM DTT unless otherwise indicated. Then samples were sonicated using a tube sonicator and boiled for 5 minutes at 95°C. SDS-PAGE was performed in MES or MOPS buffer using 4-12% NuPAGE Bis-Tris Mini Protein Gels. Proteins were transferred by Western blot on Immobilon-FL PVDF membranes by wet transfer in 20% ethanol/MOPS using Bio-Rad Mini Trans-Blot Cells or a Criterion Blotter at 400mA for at least 1.5 hours. Membranes were blocked in 5% dry milk prepared in PBS/0.02% Tween 20 for 1 hour at RT. For phospho-specific antibodies membranes were blocked and incubated with primary antibodies in 4% soy milk. Primary antibodies were added overnight at 4°C, followed by 3x washing in PBS/0.02% Tween 20, and incubation with secondary antibodies for 1 hour at RT. For quantitative detection, fluorescently labelled secondary antibodies were used with a near-infrared scanning system (Odyssey, Li-COR). Alternatively, detection was performed with horseradish peroxidase (HRP)-conjugated antibodies and Luminata Forte Western HRP Substrate or Super Signal West Femto Maximum Sensitivity Substrate on a chemiluminescence detection system (Azure Biosystem). All primary and secondary antibodies used in this study are indicated in Table S6. Related to Figures 2, 4, 5, S3 and S4.

Detection of S-sulfenylated p21

Asynchronously growing RPE-1 cells were labelled for 2 hours with 1mM BTD or 0.5% DMSO in serum-free cell culture media, then cells were washed 2x in PBS supplemented with 100U/ml catalase, trypsinised, pelleted, and lysed in buffer M (50mM HEPES pH8, 150mM NaCl, 1% SDS) supplemented with cOmplete protease and phosphatase inhibitors, 200U/ml catalase and 10mM TCEP. Cell lysates were sonicated and incubated for 30 minutes in the dark at 25°C on a horizontal shaker. Following reduction by TCEP, 40mM IAA was added, and lysates were incubated for 30 minutes as above. Then lysates were cleared by centrifugation (14,000g, 20°C for 15 minutes) and protein concentration was measured using a BSA assay. At least 1mg of protein extracts were

used for click-reaction to biotin (click buffer: 1mM CuSO4, 0.1mM TBTA, 1mM sodium ascorbate, 10nmol azide-biotin) and the click reaction was performed for 1 hour in the dark at 25°C on a horizontal shaker. Subsequently, 20mM EDTA was added, and proteins were precipitated with cloroform/methanol (Cl/MeOH) precipitation (4 volumes MeOH/ 1 volume CH3CL / 3 volumes H2O) to remove all the unreacted biotin before streptavidin enrichment. After Cl/MeOH precipitation cell pellets were resuspended in buffer S (50mM HEPES pH8, 0.5% SDS, 0.5M Urea), incubated on a horizontal shaker until the protein pellet fully dissolved (around 15 minutes), diluted 1:1 with H2O, and incubated with streptavidin sepharose over night at 4°C on a horizontal shaker. The next day, beads were washed 4x with wash buffer (50mM HEPES pH8, 4M Urea, 0.5% SDS), transferred to a new tube, washed twice with wash buffer, and once with PBS. Bound proteins were eluted by boiling for 15 minutes at 95°C in NuPAGE LDS sample buffer supplemented with 2.5mM biotin, separated by SDS-PAGE, and analysed by Western blot. Related to Figure 2.

p21-GFP pull down

For pull-down of p21-GFP recombinant GFP nanobody VHH4 [39,40] was crosslinked to carboxylic acids beads (Invitrogen) according to the manufacturer's instructions (GFP-Binder beads). To determine interactions of p21-GFP with CDK-cyclins asynchronous or G2 phase-synchronized WT and C41S #1 cells were used. G2-phase cells were treated with 10µM H_2O_2 for 30 minutes as indicated. Cells were lysed on ice for 15 minutes in buffer P (50mM Tris pH8, 100mM NaCl, 2.5mM MgCl2, 5% Glycerol, 0.5% Triton) with cOmplete protease and phosphatase inhibitors and, for reducing pull-downs only, with 10mM fresh dithiothreitol (DTT). Then lysates were cleared for 10 minutes (14,000g at 4°C), the protein concentration was determined, and at least 500µg extract added per pull-down to in buffer P-equilibrated GFP binder beads. After incubation for 1 hour on a rotation wheel at 4°C, and 3x washes in buffer P, beads were transferred into a new tube, and boiling in NuPAGE/LDS for 10 minutes at 65°C to elute proteins. Carboxylic acids beads not coupled to VHH4 were used as negative controls. Then, eluates were supplemented with 100mM DTT and analysed by SDS-PAGE and Western Blot. Related to Figures 4 and S4.

Cell cycle BTD Proteomics

RPE-1 cells were seeded at a low density (<8000 cells/cm2) into 15cm dishes and synchronised into different cell cycle phases with palbociclib and then labelled with 1mM BTD for 1 hour in serum-free media (Figure 1A). After labeling, cells were washed 2x with PBS, supplemented with 100U/ml catalase to prevent artificial oxidations during sample preparation, trypsinised, collected in PBS/catalase, and flash frozen in liquid nitrogen for later analysis. A fraction of the trypsinised cells was collected, pelleted, and fixed in ice-cold 70% EtOH for flow cytometry analysis to determine the cell cycle stage (Figure 1B). Frozen cell pellets for mass spectrometry analysis were lysed in buffer M (50mM HEPES pH 8, 150mM NaCl, 1% SDS) supplemented with HALT protease and phosphatase inhibitor cocktail, 200U/ml catalase in 50mM potassium phosphate pH=7, and 10mM TCEP, sonicated, and incubated for 30 minutes on a horizontal shaker. Next lysates were alkylated in 40mM IAA and incubated for 30 minutes as above. Lysates were pelleted and clicked to azide-Dde-biotin. For click reactions, 2.5mg lysate per time point was incubated with 25nmol of azide-picolyl-Dde-biotin in 1mM CuSO4, 0.1mM TBTA, 1mM sodium ascorbate protected from light at 20°C for 1 hour on a horizontal shaker, and reactions terminated with 20 mM EDTA for 5 minutes. Then proteins were precipitated by Cl/MeOH precipitation, pelleted (4,000 rpm for 15 minutes), washed with 4 volumes MeOH and pelleted again. Protein disks were air dried at 37°C, resuspended in 100mM Tetraethylammonium bromide (TEAB), pH8.0, and sonicated until completely dissolved. Trypsin dissolved in 0.5% formic acid was added and proteins were digested over night at 37°C on a horizontal shaker. The next day the peptides were centrifuged at 13.000rpm for 5 minutes at RT to remove insoluble material and 15ng of total digest per time point were separated for total proteome analysis. Remaining peptides of each cell cycle phase were incubated with 100ul beads / sample streptavidin sepharose ON. Then, beads were washed 2x in TEAB, resuspended in 100µl TEAB, followed by addition of TMT-18plex reagents for 1 hour at 25°C on a horizontal shaker (40µl of TMT-18plex label was dissolved in 100% acetonitrile (ACN) to a total final volume of 200µl and 20% ACN) and termination of the labeling reaction by 5% hydroxylamine. Then, beads were washed 2x with TEAB buffer supplemented with 500mM NaCl and 0.5% SDS and combined. After 3 further washes in TEAB buffer, and 2x times in water, peptides were eluted via cleavage

of the Dde-group on biotin 2% hydrazine at 20°C for 30 minutes on a horizontal shaker. The eluate was collected, cleaned from beads using TopTips, dried, and processed for mass spectrometry injection. Peptides taken for total proteome analysis were labelled according to manufactures instructions with TMT-18plex. Related to Figures 1 and S1.

p21-Oxidation Stoichiometry

RPE-1 cells were synchronised in G2 phase, washed with PBS, trypsinised, quenched with complete media, washed once with PBS, separated into two equal samples (total cysteine vs. oxidized cysteine) in PBS, pelleted, and flash frozen for subsequent analysis. Then, cells were lysed in buffer M2 (100mM TEAB, pH8.5, 150mM NaCl, 1% sodium deoxycholate, 1mM EDTA, 10µM neocuproine) supplemented with fresh cOmplete protease/phosphatase inhibitors and 200U/mL catalase. For the total cysteine sample the lysis buffer was immediately supplemented with 10mM TCEP, for oxidized cysteine samples with 10mM IAA. H_2O_2 samples cells were lysed in buffer M2 containing 10 or 100µM H_2O_2 and incubated for 10 minutes. Subsequently, 200U/ml catalase and either 10mM TCEP (total cysteines) or 10mM IAM (oxidized cysteines) were added. All samples were homogenised using a tube sonicator and incubated for 1 hour at 37°C protected from light. Protein concentration was determined, and 500µg/sample was taken for further processing. Next, reactive IAA and TCEP were quenched by 10mM L-Cysteine, followed by simultaneous reduction and alkylation with 40mM IPM for 1 hour at 37°C protected from light. Proteins were added to in M2 buffer equilibrated carboxylic acids beads (Invitrogen) coupled to VHH4[39,40]. After 1 hour on a rotating wheel on 4°C beads were washed 3x with buffer M supplemented with 500mM NaCl, transferred to a new tube, washed twice more with buffer M2, and resuspended in 100mM TEAB digest with 50ng/µl trypsin ON. Digested peptides were collected, and TMT labelled (TMT-10plex) according to manufactures instructions. Related to Figure 2.

Mass Spectrometry Analysis, Data Search, and Quantification

TMT labelled peptides for total proteome analysis were fractionated with high-pH Reversed-Phase (RP) chromatography using the XBridge C18 column (2.1 × 150 mm, 3.5 µm, Waters) on an UltiMate 3000 HPLC system. Mobile phase A was 0.1% (v/v) ammonium hydroxide and mobile phase B was ACN, 0.1% (v/v) ammonium hydroxide.

The peptides were fractionated at 0.2 mL/min with the following gradient: 5 minutes at 5% B, up to 12% B in 3 min, for 32 min gradient to 35% B, gradient to 80% B in 5 min, isocratic for 5 minutes and re-equilibration to 5% B. Fractions were collected every 42 sec SpeedVac dried and eventually pooled into 30 samples for LC-MS analysis. The TMT labelled peptides from p21 pull-downs were fractionated with a 1×100 mm RP column at 70 µL/min and 8 fractions were eventually collected for LC-MS analysis.

LC-MS analysis for the BTD and total proteome experiments was performed on an UltiMate 3000 UHPLC system coupled with the Orbitrap Lumos mass spectrometer (Thermo Scientific). Peptides were loaded onto the Acclaim PepMap 100, 100 µm × 2 cm C18, 5 µm, trapping column at flow rate 10 µL/min and analysed with an Acclaim PepMap (75 µm × 50 cm, 2 µm, 100 Å) C18 capillary column connected to a stainless-steel emitter on the EASY-Spray source. Mobile phase A was 0.1% formic acid and mobile phase B was 80% ACN, 0.1% formic acid. Peptides were analysed with a gradient of 5%-38% B in 125 min (BTD runs) or 95 min (total proteome runs). MS scans were acquired in the range of 375-1,500 m/z at a mass resolution of 120,000. Precursors were selected with the top speed mode in 3 sec cycles and isolated for HCD fragmentation at 30k or 50k resolution with 36% collision energy (CE). Targeted precursors were dynamically excluded for 30 or 45 seconds with 7 ppm mass tolerance.

The analysis of the p21 pull-downs (IPM experiment) was performed on an Orbitrap Ascend mass spectrometer (Thermo Scientific) with a Synchronous Precursor Selection MS3 method over a 100 min gradient (3%-27% B) using the nanoE MZ PST BEH130 C18, 1.7 µm, 75 µm × 250 mm analytical column (Waters). MS2 spectra were collected with HCD fragmentation (CE=32%) and ion trap detection whilst the MS3 quantification spectra were collected with HCD fragmentation (CE=55%) and Orbitrap detection at 45k resolution. The mass spectra were processed in Proteome Discoverer (Thermo Scientific) v2.4 for the total proteome data or v3.0 for the BTD and p21 pull-downs with the SequestHT and Comet for v3.0, search engines for peptide identification and quantification. For the BTD and total proteome experiments the precursor and fragment ion mass tolerances were 20 ppm and 0.02 Da respectively. For the p21 pull-downs MS2 tolerance was 0.5 Da. Spectra were searched for fully tryptic peptides with maximum 2 missed cleavages. TMTpro or TMT6plex at N-terminus/K were selected as static modifications according to each experimental design. Oxidation of M and deamidation

of N/Q were selected as dynamic modifications in all searches. Additionally, for the BTD experiments, BTD+DdePicolyAzide_Cleaved (+481.153 Da) and Carbamidomethyl (+57.021 Da) at C were selected as dynamic modifications. Carbamidomethyl at C was set as static for the total proteome data. For the p21 pull-downs, IPM (+95.03711) and Carbamidomethyl at C were added as dynamic modifications. Spectra were searched against reviewed UniProt Homo Sapiens protein entries; peptide confidence was estimated with the Percolator node and peptides were filtered at q-value<0.01 based on target-decoy database search. The reporter ion quantifier node included a TMTpro or TMT6plex quantification method with an integration window tolerance of 15 ppm. Related to Figures 1, 2 and S1.

Statistical analysis of proteomics data

For the BTD data, raw peptide abundances (S/N) were normalized by sample median, log2 transformed and centred at zero per replicate batch. The mean and standard deviation were calculated across all biological and technical replicates. For the total proteome data, the normalized abundances were exported from Proteome Discoverer, log2 transformed, centred at zero per replicate batch and averaged across the two biological replicates. The mean BTD data were then corrected for the mean total protein changes across the time points using linear regression. The protein data were the independent variable (x) whilst the BTD data were the dependent variable (y) per peptide across time points; the residuals of the linear regressions were the BTD changes not attributed to total protein changes. To identify peptides with maximum change at G2/M, S and G1 cell cycle phases, Pearson correlation coefficients and p-values were calculated against defined binary reference profiles in Excel by calculating the t-statistic and using the T.DIST.2T function. Related to Figures 1, 2 and Table S1.

Imaging

Automated microscopy was performed on an ImageXpress Micro Confocal system in wide-field mode (Molecular Devices) equipped with 10x, 0.45 NA and 20x, 0.7 NA Plan Apo air objectives (Nikon) and laser-based autofocus. Excitation and detection were done by a Spectra X light engine (Lumencor) and 16 bit sCMOS (Andor) camera with the indicated filters: DAPI (Ex: 377/54; Dic: 409, Em:447/60); FITC/GFP (Ex: 475/34; Dic: 506;

Em: 536/40); TexasRed (Ex: 560/32 Dic: 593; Em: 593/40) and Cy5 (Ex: 631/28; Dic: 660; Em: 624/40) using binning =1. In live cell experiments the cells were maintained in a stage incubator at 37 °C in a humidified atmosphere of 5% CO_2 and a single position per well was imaged. Imaging was performed in phenol red-free DMEM supplemented with 10% (v/v) FBS, 1% (v/v) penicillin-streptomycin, 1% Glutamax, 0.5ug/ml Amphotericin B and 0.26% sodium bicarbonate. For immunofluorescence imaging at least 9 positions per well acquired with binning = 1. All cells were grown in black 96 well clear-bottom plates (µclear, Greiner Bio-One). For crystal-violet imaging a scanning system (Odyssey, Li-COR) supplied with RGB-Trans option was used. β-galactosidase and DAPI stained cells grown in black 96 well clear-bottom plates were imaged on an EVOS M5000 imaging system (Thermo Fisher) supplied with an RGB Trans option that generates colour images from interlaced RGB images. Images were taken with a 10x objective/NA 0.30 detecting DAPI (tagBFP filter cube) and β-galactosidase staining (tagBFP, GFP, TexasRed filter cubes) intensities. At least two randomly selected positions per well were imaged. BTD labelled sulfenic acids were imaged in fixed cells grown in IBIDI-chambers on a Delta Vision wide-field deconvolution fluorescence microscope equipped with a PCO Edge/sCMOS camera (Imsol) at binning = 1, an Olympus UPlan Apo 20X/NA 0.7 lens (Olympus) objective, and DAPI (381-412) and Cy5 (625-646). Related to Figures 3-6, S1, S3-S5.

Semi-Automated Image Analysis, Immune Fluorescence Staining

Image analyses of IF images collected on the ImageXpress were performed by automated pipelines developed in the Custom Module Editor of the MetaXpress software (Molecular devices). Briefly, images were flat-field and background corrected using a top-hat filter, nuclei were segmented based on Hoechst 33342 staining to create nuclear masks, which were used to extract fluorescence signals for p21-GFP, pRb 807/811, and gH2AX. Hoechst 33342 staining was also used detect and create masks for micronuclei based on intensity and size thresholds. γH2AX-positive, pRb-positive, or p21-positive cells were filtered by applying a threshold to gH2AX-Cy5, pRb-Cy5, or p21-GFP flat-field corrected images based on visibility by eye. All treatments and cell lines were processed within the same imaging experiments with the same thresholds. For single-cell analysis,

single-cell data of integrated p21-intensity, integrated-pRb intensities, and integrated Hoechst-33342 intensities were extracted.
Related to Figures 3, 5, 6, S3 and S5.

Image analysis of β-galactosidase and crystal-violet staining

To determine β-galactosidase staining per cell we used a Fiji-plugin developed by[61] . Cells irradiated with 6Gy were used to determine threshold intensities, which were then applied automatically to all images. Simultaneous counting of cells (DAPI) was used to divide the Intensity signal by the number of cells. To measure integrated densities of crystal-violet stained cells images were loaded into Fiji-ImageJ2 (version 2.14.0/1.54f) and converted to RGB images. Integrated densities of the whole well were measured and subtracted from background signals. Related to Figure 6.

Semi-automated Image Analysis of Live Cell Imaging

Semi-automated image analysis was implemented using custom ImageJ macros, Jython and Python scripts. Image background subtraction and illumination correction were performed with the BaSIC[82]. As G0 cell nuclei are negative for mRuby-PCNA, a pseudo-channel, merging p21-GFP and mRuby-PCNA channels, was used for segmentation. Additionally, as S phase replication foci (mRuby-PCNA) can lead to over segmentation, StarDist segmentation[83] was performed on Ilastik[84] pixel probability maps, trained to delineate "nuclei" and "background" classes, from the p21-GFP + mRuby-PCNA pseudo-channel. Objects were linked through time using linear assignment problem algorithm in TrackMate[85], and tracks present for less than 24 hrs were filtered out. Before feature extraction, tracks were manually curated to only include tracks with one S/G2 transition and one mitotic event. Tracks were terminated for one of three reasons: (1) transition from G1 to S, (2) migration out of frame, or (3) loss of track due to segmentation/tracking error. Following feature extraction analysis and presentation was performed using the Python libraries, Pandas and Matplotlib. All track features were smoothed with a +/-2 rolling mean filter. From the curated tracks in silico synchronisation was performed at the S/G2 transition, defined as the frame where mRuby-PCNA intensity standard deviation was highest. Mitosis was also classified as the frame where object area was greatest (within a lenient range of 2-20 hours post mitosis), representing the release of nuclear mRuby-

PCNA into the cytoplasm at nuclear envelope breakdown. G2 timepoint measurements were taken at the midpoint between the S/G2 transition and M. G1 timepoint measurements were taken 3 hrs post mitosis (Figure S4M). Related to Figures 4 and S4.

Data Visualization

Fluorescence or scanned images (crystal-violet and Western Blot) were processed with Fiji (version 2.14.0/1.54f) [86] and identical brightness and contrast settings were applied per channel to images within the same experiment. p21-sulfenylation across the cell cycle was visualized with CytoScape ([87], version 3.1). Scatter plots, bar charts, and XY plots were visualized with Prism 10.0 (GraphPad). Bivariate density plots and GO analysis with R studio (2024.04.2+764, R version 4.4.1) using libraries tidyverse, ggpointdensity, ggplot2, and gprofiler2. In all density plots the same number of cells was blotted. Single and mean p21-intensities from time-lapse imaging were plotted with Python version (3.11.4).

Structures and protein conservation

ChimeraX software ([88], version: 1.6.1) was used to illustrate the publicly available structures of p21 with CyclinD-CDK4 (PDB: 6p8h[34]) or model of p21 with CyclinA-CDK2[35]. The distances of p21 to Cyclin-CDK proteins were measured using ChimeraX distance calculator. Assessment of protein conservation was performed using ProViz software[79]. To compare the conservation of p21 sequences with proteins from the same family the online version of Clustal-omega software[89] was used for alignment. Related to Figure 2, S2.

Statistical analysis

Statistical analysis was performed using Prism 10 (GraphPad) using the statistical tests indicated in the figure legends. n denote the number of biological repeats, N the number of measurements within the analysis. All experiments were performed at least three times unless otherwise indicated in the figure legends. p values are indicated in the figures and p values lower or equal 0.05 were considered as statistically significant. For quantitative Western Blot analyses, the intensity values were first normalized to the loading control and then to the experimental control.

Table S2:

Cell lines used in this study.

ID	Name	Parental Cell line	Insert/reagent	Reference
CL1	RPE-1 FRT/TO	NA	NA	RRID:CVCL_VP32
CL2	RPE-1 FRT/TO, mRuby-PCNA, p21-GFP	NA	NA	[21]
CL3	RPE-1 FRT/TO, mRuby-PCNA, p21-GFP C41S #1	2	RD1, RD2, RD3, RD4, RD5 Table S3	This study
CL4	RPE-1 FRT/TO, mRuby-PCNA, p21-GFP C41S #2	2	RD1, RD2, RD3, RD4, RD5 Table S3	This study
CL5	RPE-1 FRT/TO, mRuby-PCNA, p21-GFP, Tet ON HA-VHH4-TRX WT	2	PL4, PL6 Table S4	This study
CL6	RPE-1 FRT/TO, mRuby-PCNA, p21-GFP, Tet ON HA-VHH4-TRX mut	2	PL5, PL6 Table S4	This study
CL7	RPE-1 FRT/TO, mRuby-PCNA, p21-GFP C41S #1, Tet ON HA-VHH4-TRX WT	3	PL4, PL6 Table S4	This study
CL8	RPE-1 FRT/TO, mRuby-PCNA, p21-GFP C41S #1, Tet ON HA-VHH4-TRX mut	3	PL5, PL6 Table S4	This study

Table S3:

gRNA and repair templates sequences used for genome editing of CDKN1A.

* denotes phosphorothioated nucleotides.

ID	Type	Gene	Sequence 5'-3'
RD1	gRNA	ATPA1A	GAGTTCTGTAATTCAGCATA (Agudelo et al, 2017)
RD2	gRNA	CDKN1A	CGACTGTGATGCGCTAATGG
RD3	gRNA	CDKN1A	GCTAATGGCGGGCTGCATCC
RD4	ssODN	ATP1A1	C*A*ATGTTACTGTGGATTGGAGCGATTCTTTGTTTCTTGG CTTATAGCATCAGAGCTGCTACAGAAGAGGAACCTCAAA ACGATGACGTGAGTTCTGTAATTCAGCATATCGATTTGTA GTACACATCAGATATC*T*T
RD5	ssODN	p21	G*A*A*CCCATGCGGCAGCAAGGCCTGCCGCCGCCTCTT CGGCCCAGTGGACAGCGAGCAGCTGAGCCGCGACTGT GATGCGCTAATGGCCGGCAGCATCCAAGAGGCTCGAGA GCGATGGAACTTCGACTTTGTCACCGAGACACCACTGGA GGGTGACTTCGCCTGGGAGCGTGTGCGGGGCCTTGGC CTGCCCAAGC*T*C*T

Table S4:

List of all plasmids used in this study. TBD = to be deposited

ID	Plasmid name	Created by
PL1	eSPCas9.1-ATP1A1-G3_sgRNA1(BbsI)	Addgene: 86613
PL2	eSPCas9.1-ATP1A1-G3_sgRNA1(BbsI) + sgRNA2(BsmBI)	This study, Addgene: TBD
PL3	eSPCas9.1-ATP1A1-G3_sgRNA1(p21-gRNA1) + sgRNA2(p21-gRNA2)	This study, Addgene: TBD
PL4	pCDNA5 FRT/TO HA-VHH4-TRX WT	This study, Addgene: TBD
PL5	pCDNA5 FRT/TO HA-VHH4-TRX C32S/C35S (mut)	This study, Addgene: TBD
PL6	pOG44	Invitrogen, V600520

Table S5:

PCR primer sequences used in this study. FWD = forward, REV = reverse used to amplify genomic DNA sequence of CDKN1A. Barcode underlined and in bold.

ID	Orientation	Sequence 5'-3'
PCR1	FWD	AGTGTCTAATCTCCGCCGTGACCAG
PCR2	REV	GTCCGCACCTGTCATGCTGG
PCR3	FWD; Barcode	TAGC**CGATGT**AGAACCGGCTGGGGATGTCC
PCR4	FWD; Barcode	TAGC**TTAGGC**AGAACCGGCTGGGGATGTCC
PCR5	FWD; Barcode	TAGC**TGACCA**AGAACCGGCTGGGGATGTCC
PCR6	FWD; Barcode	TAGC**ACAGTG**AGAACCGGCTGGGGATGTCC
PCR7	FWD; Barcode	TAGC**GCCAAT**AGAACCGGCTGGGGATGTCC
PCR8	FWD; Barcode	TAGC**CAGATC**AGAACCGGCTGGGGATGTCC
PCR9	REV	TCGACCCTGAGAGTCTCCAGGTC

Table S6:

List of all antibodies used in this study.

Antibody	Company	Cat.no:	Dilution	Raised in:
Primary Antibodies				
Actin	Sigma	A5441	1:5000	Mouse
CDK1	Cell Signalling	9116	1:1000	Mouse
CDK2	Santa Cruz	Sc6248	1:500	Mouse
CDK4	Cell Signalling	12790	1:1000	Rabbit
Cyclin A2	Santa Cruz	Sc-596	1:500	Rabbit
Cyclin B1	Santa Cruz	Sc-245	1:1000	Mouse
Cyclin D1	Santa Cruz	Sc-20044	1:200	Mouse
gH2AX	Sigma	05-636-I	1:1000	Mouse
GFP	Abcam	Ab6673	1:1000	Goat
GAPDH	Cell Signalling	2118	1:5000	Rabbit
HA-tag	Moravian	NA	1:5000	Mouse
p21	Cell Signalling	2947	1:1000	Rabbit
pRb (Ser807/811)	Cell Signalling	8516	1:10000	Rabbit
RPL26	Bethyl	A300-686A	1:2000	Rabbit
TP53	Santa Cruz	sc-126	1:1000	Mouse
Total Rb	Cell Signalling	9309	1:5000	Mouse
Secondary Antibodies				
AlexaFluor647 Donkey anti rabbit	Thermo Fisher	A-31573	1:1000	Donkey
AlexaFluor647 Donkey anti mouse	Thermo Fisher	A-31571	1:1000	Donkey
anti-mouse, HRP-linked antibody	Cell Signalling	7076	1:1000	Goat
anti-rabbit, HRP-linked antibody	Cell Signalling	7074	1:1000	Goat
IRDye 680RD donkey anti mouse	Li-Cor	926-68072	1:5000	Donkey
IRDye 680RD donkey anti rabbit	Li-Cor	926-68073	1:5000	Donkey
IRDye 800CW donkey anti mouse	Li-Cor	926-32212	1:5000	Donkey
IRDye 800CW donkey anti rabbit	Li-Cor	926-32213	1:5000	Donkey

Table S7:

All reagents used in this study

Reagents	Company	Cat.No
Acetonitrile	Sigma	75-05-8
Amphotericin B	Sigma	1397-89-3
Azide-488	Jena Bioscience	CLK-1276-1
Azide-647	Jena Bioscience	CLK-1299-1
Azide-Dde Biotin	Click Chemistry Tools	1186-25
β-Galactosidase Staining Kit	Cell Signalling	9860
BSA	Sigma	A3294
Catalase	Sigma	C3155
Carboxylic acid beads (Dynabeads)	Thermo Fisher	65012
Chloroform	Sigma	366927
Criterion Blotter.	Biorad	1704070
Crystal-violet	Sigma	C3886
CuSO4	Thermo Fisher	A13986.0I
DAPI	Sigma	D9542
DMSO	Sigma	D2650
Dublecco's Modifies Eagle Medium/Nutrient Mixture F-12 Ham	Thermo Fisher	31330095
Dry Milk	Roth	T145.3
DTT	Merck	R0861
E.Z.N.A. Cycle Pure Kit	VWR	D6492-00
E.Z.N.A. Gel Extraction Kit	VWR	D2500-01
E.Z.N.A Genomic Extraction Kit	VWR	D3396-02
E.Z.N.A. Plasmid Mini Kit	VWR	D6942-02
EDTA	Calbiochem	324503
Ethanol	VWR	100983
Fetal Bocine Serum (FBS) TET free	Gibco	N.A.
Formic Acid	Sigma	64-18-6
Glutamax	Thermo Fisher	35050061
Glycerol 40%	VWR	10118
H_2O_2	Sigma	L14000.AP
HALT protease and phosphatase inhibitor cocktail	Thermo Fisher	78441
HEPES	Sigma	H6147
Hoechst-33342	Invitrogen	H3570
Hydrazine	Sigma	207942-100G

--- continued on next page ---

Reagents	Company	Cat.No
Hydroxylamine	Thermo Fisher	90115
IAA	Sigma	I6125
IBIDI Slides 8wells	IBIDI	80826
Immobilon-FL DVDF Membranes	Merck	IPFL00010
MES Buffer	Lifetech	NP0002
Mini Trans-Blot Cell	Bio-Rad	1703930
Methanol	VWR	P20847
$MgCl_2$	VWR International	10149
MOPS Buffer	Carl Roth	NP0001
NaCl	VWR International	10241
Neon Transfection System	Thermo Fisher	N.A.
Mark12 protein standard	Thermo Fisher	LC5677
NuPage LDS Buffer	Thermo Fisher	NP0008
Nutlin-3	Sigma	N6287
Ouabain	Sigma	O3125
Palbociclib	Selleckchem	S1116
Penicilin 10,000U/Ml-Streptomycin 10,000µg/Ml	Sigma	P0781
PFA 16%	Thermo Fisher	28906
Phosphatase Inhibitors	Roche	4906845001
Phosphate Buffer Saline (PBS)	VWR International	10203
Ponceau	VWR	J60744
Propidium Iodide	Invitrogen	P3566
Protease Inhibitors	Roche	11206893001
Proteinase K	NEB	P8107S
Rnase A	Thermo Fisher	R1253
SDS	VWR	837
Sodium Ascorbate	Thermo Fisher	A17759.22
Sodium Bicarbonate	Thermo Fisher	25080094
Soy Milk	Vitasyg	NA
Streptavidin Sepharose High Performance	Sigma	17-5113-01
Super Signal West Femto Maximum Sensitivity Substrate	Thermo Fisher	34095
TBTA	Sigma	678937
TCEP	Thermo Fisher	77720
TEAB Buffer	Thermo Fisher	90114
Tetracycline	Affymetrix	22105
TMT-10plex	Thermo Fisher	90110

--- continued on next page ---

Reagents	Company	Cat.No
TMT-18plex	Thermo Fisher	A52045
Toptips	Polylc INC	410.992.5400
Tris pH8	Calbiochem	648311
Triton X-100	Thermo Fisher	9002-93-1
Trypsin For Cell Culture	Sigma	T4174
Trypsin For MS	Thermo Fisher	90059
Tween-20	VWR	M147-1L

References

1. Sies H, Jones DP. Reactive oxygen species (ROS) as pleiotropic physiological signalling agents. Nat Rev Mol Cell Biol. 2020;21(7):363-383. doi:10.1038/s41580-020-0230-3

2. Corcoran A, Cotter TG. Redox regulation of protein kinases. FEBS Journal. 2013;280(9):1944-1965. doi:10.1111/febs.12224

3. Holmström KM, Finkel T. Cellular mechanisms and physiological consequences of redox-dependent signalling. Nat Rev Mol Cell Biol. 2014;15(6):411-421. doi:10.1038/nrm3801

4. Tsuchiya Y, Byrne DP, Burgess SG, et al. Covalent Aurora A regulation by the metabolic integrator coenzyme A. Redox Biol. 2020;28. doi:10.1016/j.redox.2019.101318

5. Reddie KG, Carroll KS. Expanding the functional diversity of proteins through cysteine oxidation. Curr Opin Chem Biol. 2008;12(6):746-754. doi:10.1016/j.cbpa.2008.07.028

6. Ivanova JS, Pugovkina NA, Neganova IE, Kozhukharova I V., Nikolsky NN, Lyublinskaya OG. Cell Cycle-Coupled Changes in the Level of Reactive Oxygen Species Support the Proliferation of Human Pluripotent Stem Cells. Stem Cells. 2021;39(12):1671-1687. doi:10.1002/stem.3450

7. Kirova DG, Judasova K, Vorhauser J, et al. A ROS-dependent mechanism promotes CDK2 phosphorylation to drive progression through S phase. Dev Cell. 2022;57(14):1712-1727.e9. doi:10.1016/j.devcel.2022.06.008

8. Patterson JC, Joughin BA, van de Kooij B, Lim DC, Lauffenburger DA, Yaffe MB. ROS and Oxidative Stress Are Elevated in Mitosis during Asynchronous Cell Cycle Progression and Are Exacerbated by Mitotic Arrest. Cell Syst. 2019;8(2):163-167.e2. doi:10.1016/j.cels.2019.01.005

9. Menon SG, Goswami PC. A redox cycle within the cell cycle: Ring in the old with the new. Oncogene. 2007;26(8):1101-1109. doi:10.1038/sj.onc.1209895

10. Amponsah PS, Yahya G, Zimmermann J, et al. Peroxiredoxins couple metabolism and cell division in an ultradian cycle. Nat Chem Biol. 2021;17(April). doi:10.1038/s41589-020-00728-9

11. López-Grueso MJ, Lagal DJ, García-Jiménez ÁF, et al. Knockout of PRDX6 induces mitochondrial dysfunction and cell cycle arrest at G2/M in HepG2 hepatocarcinoma cells. Redox Biol. 2020;37. doi:10.1016/j.redox.2020.101737

12. Smith-Pearson PS, Kooshki M, Spitz DR, Poole LB, Zhao W, Robbins ME. Decreasing peroxiredoxin II expression decreases glutathione, alters cell cycle distribution, and sensitizes glioma cells to ionizing radiation and H2O2. Free Radic Biol Med. 2008;45(8):1178-1189. doi:10.1016/j.freeradbiomed.2008.07.015

13. Fu L, Liu K, Ferreira RB, Carroll KS, Yang J. Proteome-Wide Analysis of Cysteine S-Sulfenylation Using a Benzothiazine-Based Probe. Curr Protoc Protein Sci. 2019;95(1):e76. doi:10.1002/cpps.76

14. Takahashi M, Chong HB, Zhang S, et al. DrugMap: A quantitative pan-cancer analysis of cysteine ligandability. Cell. 2024;187(10):2536-2556.e30. doi:10.1016/j.cell.2024.03.027

15. Xiao H, Jedrychowski MP, Schweppe DK, et al. A Quantitative Tissue-Specific Landscape of Protein Redox Regulation during Aging. Cell. 2020;180(5):968-983.e24. doi:10.1016/j.cell.2020.02.012

16. Byrne DP, Shrestha S, Galler M, et al. Aurora A regulation by reversible cysteine oxidation reveals evolutionarily conserved redox control of Ser/Thr protein kinase activity. Sci Signal. 2020;13(639):2713. doi:10.1126/scisignal.aax2713

17. Lim DC, Joukov V, Rettenmaier TJ, et al. Redox priming promotes Aurora A activation during mitosis. Sci Signal. 2020;13(641):6707. doi:10.1126/scisignal.abb6707

18. Knight H, Abis G, Kaur M, et al. Cyclin D-CDK4 Disulfide Bond Attenuates Pulmonary Vascular Cell Proliferation. Circ Res. 2023;133(12):966-988. doi:10.1161/CIRCRESAHA.122.321836

19. Min M, Spencer SL. Spontaneously slow-cycling subpopulations of human cells originate from activation of stress-response pathways. Coller HA, ed. PLoS Biol. 2019;17(3):e3000178. doi:10.1371/journal.pbio.3000178

20. Spencer SL, Cappell SD, Tsai FC, Overton KW, Wang CL, Meyer T. The Proliferation-Quiescence Decision Is Controlled by a Bifurcation in CDK2 Activity at Mitotic Exit. Cell. 2013;155(2):369-383. doi:10.1016/j.cell.2013.08.062

21. Barr AR, Cooper S, Heldt FS, et al. DNA damage during S-phase mediates the proliferation-quiescence decision in the subsequent G1 via p21 expression. Nat Commun. 2017;8(1):14728. doi:10.1038/ncomms14728

22. Wesley Overton K, Spencer SL, Noderer WL, Meyer T, Wang CL. Basal p21 controls population heterogeneity in cycling and quiescent cell cycle states. Proc Natl Acad Sci U S A. 2014;111(41):E4386-E4393. doi:10.1073/pnas.1409797111

23. Bornstein G, Bloom J, Sitry-Shevah D, Nakayama K, Pagano M, Hershko A. Role of the SCFSkp2 ubiquitin ligase in the degradation of p21Cip1 in S phase. Journal of Biological Chemistry. 2003;278(28):25752-25757. doi:10.1074/jbc.M301774200

24. Huang Y, Yoon MK, Otieno S, Lelli M, Kriwacki RW. The Activity and Stability of the Intrinsically Disordered Cip/Kip Protein Family Are Regulated by Non-Receptor Tyrosine Kinases. J Mol Biol. 2015;427(2):371-386. doi:10.1016/j.jmb.2014.11.011

25. Zhu H, Nie L, Maki CG. Cdk2-dependent Inhibition of p21 Stability via a C-terminal Cyclin-binding Motif. Journal of Biological Chemistry. 2005;280(32):29282-29288. doi:10.1074/jbc.M407352200

26. Gupta V, Yang J, Liebler DC, Carroll KS. Diverse Redoxome Reactivity Profiles of Carbon Nucleophiles. J Am Chem Soc. 2017;139(15):5588-5595. doi:10.1021/jacs.7b01791

27. Francois L, Boskovic P, Knerr J, et al. BCAT1 redox function maintains mitotic fidelity. Cell Rep. 2022;41(3). doi:10.1016/j.celrep.2022.111524

28. Trotter EW, Hagan IM. Release from cell cycle arrest with Cdk4/6 inhibitors generates highly synchronized cell cycle progression in human cell culture. Open Biol. 2020;10(10). doi:10.1098/rsob.200200

29. Thompson A, Schäfer J, Kuhn K, et al. Tandem Mass Tags: A Novel Quantification Strategy for Comparative Analysis of Complex Protein Mixtures by MS/MS. Anal Chem. 2003;75(8):1895-1904. doi:10.1021/ac0262560

30. Talwar D, Miller CG, Grossmann J, et al. The GAPDH redox switch safeguards reductive capacity and enables survival of stressed tumour cells. Nat Metab. 2023;5(4):660-676. doi:10.1038/s42255-023-00781-3

31. Chen J, Jackson PK, Kirschner MW, Dutta A. Separate domains of p21 involved in the inhibition of Cdk kinase and PCNA. Nature. 1995;374(6520):386-388. doi:10.1038/374386a0

32. Kriwacki RW, Hengst L, Tennant L, Reed SI, Wright PE. Structural studies of p21Waf1/Cip1/Sdi1 in the free and Cdk2-bound state: conformational disorder mediates binding diversity. Proceedings of the National Academy of Sciences. 1996;93(21):11504-11509. doi:10.1073/pnas.93.21.11504

33. Nakanishi M, Robetorye RS, Adami GR, Pereira-Smith OM, Smith JR. Identification of the active region of the DNA synthesis inhibitory gene p21Sdi1/CIP1/WAF1. EMBO J. 1995;14(3):555-563. doi:10.1002/j.1460-2075.1995.tb07031.x

34. Guiley KZ, Stevenson JW, Lou K, et al. p27 allosterically activates cyclin-dependent kinase 4 and antagonizes palbociclib inhibition. Science (1979). 2019;366(6471). doi:10.1126/science.aaw2106

35. Swadling JB, Warnecke T, Morris KL, Barr AR. Conserved Cdk inhibitors show unique structural responses to tyrosine phosphorylation. Biophys J. 2022;121(12):2312-2329. doi:10.1016/J.BPJ.2022.05.024

36. Gregoret LM, Rader SD, Fletterick RJ, Cohen FE. Hydrogen bonds involving sulfur atoms in proteins. Proteins: Structure, Function, and Bioinformatics. 1991;9(2):99-107. doi:10.1002/prot.340090204

37. Mészáros B, Erdős G, Dosztányi Z. IUPred2A: context-dependent prediction of protein disorder as a function of redox state and protein binding. Nucleic Acids Res. 2018;46(W1):W329-W337. doi:10.1093/nar/gky384

38. Li X, Gluth A, Zhang T, Qian WJ. Thiol redox proteomics: Characterization of thiol-based post-translational modifications. Proteomics. 2023;23(13-14). doi:10.1002/pmic.202200194

39. Rothbauer U, Zolghadr K, Tillib S, et al. Targeting and tracing antigens in live cells with fluorescent nanobodies. Nat Methods. 2006;3(11):887-889. doi:10.1038/nmeth953

40. Saerens D, Pellis M, Loris R, et al. Identification of a Universal VHH Framework to Graft Non-canonical Antigen-binding Loops of Camel Single-domain Antibodies. J Mol Biol. 2005;352(3):597-607. doi:10.1016/j.jmb.2005.07.038

41. Zerjatke T, Gak IA, Glauche I, Rg J, Correspondence M. Quantitative Cell Cycle Analysis Based on an Endogenous All-in-One Reporter for Cell Tracking and Classification. CellReports. 2017;19:1953-1966. doi:10.1016/j.celrep.2017.05.022

42. Agudelo D, Duringer A, Bozoyan L, et al. Marker-free coselection for CRISPR-driven genome editing in human cells. Nat Methods. 2017;14(6):615-620. doi:10.1038/nmeth.4265

43. Ezhevsky SA, Ho A, Becker-Hapak M, Davis PK, Dowdy SF. Differential Regulation of Retinoblastoma Tumor Suppressor Protein by G 1 Cyclin-Dependent Kinase Complexes In Vivo. Mol Cell Biol. 2001;21(14):4773-4784. doi:10.1128/MCB.21.14.4773-4784.2001

44. Mittnacht S, Lees JA, Desai D, Harlow E, Morgan DO, Weinberg RA. Distinct sub-populations of the retinoblastoma protein show a distinct pattern of phosphorylation. EMBO J. 1994;13(1):118-127. doi:10.1002/j.1460-2075.1994.tb06241.x

45. Narasimha AM, Kaulich M, Shapiro GS, Choi YJ, Sicinski P, Dowdy SF. Cyclin D activates the Rb tumor suppressor by mono-phosphorylation. Elife. 2014;3. doi:10.7554/eLife.02872

46. Arora M, Moser J, Hoffman TE, et al. Rapid adaptation to CDK2 inhibition exposes intrinsic cell-cycle plasticity. Cell. 2023;186(12):2628-2643.e21. doi:10.1016/j.cell.2023.05.013

47. Kim S, Leong A, Kim M, Yang HW. CDK4/6 initiates Rb inactivation and CDK2 activity coordinates cell-cycle commitment and G1/S transition. Sci Rep. 2022;12(1):16810. doi:10.1038/s41598-022-20769-5

48. Pennycook BR, Barr AR. Palbociclib-mediated cell cycle arrest can occur in the absence of the CDK inhibitors p21 and p27. Open Biol. 2021;11(11). doi:10.1098/rsob.210125

49. Li J, Cai Z, Vaites LP, et al. Proteome-wide mapping of short-lived proteins in human cells. Mol Cell. 2021;81(22):4722-4735.e5. doi:10.1016/j.molcel.2021.09.015

50. Bashir T, Dorrello NV, Amador V, Guardavaccaro D, Pagano M. Control of the SCFSkp2–Cks1 ubiquitin ligase by the APC/CCdh1 ubiquitin ligase. Nature. 2004;428(6979):190-193. doi:10.1038/nature02330

51. Wei W, Ayad NG, Wan Y, Zhang GJ, Kirschner MW, Kaelin WG. Degradation of the SCF component Skp2 in cell-cycle phase G1 by the anaphase-promoting complex. Nature. 2004;428(6979):194-198. doi:10.1038/nature02381

52. Dulić V, Stein GH, Far DF, Reed SI. Nuclear Accumulation of p21 Cip1 at the Onset of Mitosis: a Role at the G 2 /M-Phase Transition. Mol Cell Biol. 1998;18(1):546-557. doi:10.1128/MCB.18.1.546

53. Krenning L, Feringa FM, Shaltiel IA, vandenBerg J, Medema RH. Transient activation of p53 in G2 phase is sufficient to induce senescence. Mol Cell. 2014;55(1):59-72. doi:10.1016/j.molcel.2014.05.007

54. Müllers E, Cascales HS, Jaiswal H, Saurin AT, Lindqvist A. Nuclear translocation of Cyclin B1 marks the restriction point for terminal cell cycle exit in G2 phase. Cell Cycle. 2014;13(17):2733-2743. doi:10.4161/15384101.2015.945831

55. Vassilev LT, Vu BT, Graves B, et al. In Vivo Activation of the p53 Pathway by Small-Molecule Antagonists of MDM2. Science (1979). 2004;303(5659):844-848. doi:10.1126/science.1092472

56. Hass DT, Zhang Q, Autterson GA, Bryan RA, Hurley JB, Miller JML. Medium Depth Influences O2 Availability and Metabolism in Human RPE Cultures. Investigative Opthalmology & Visual Science. 2023;64(14):4. doi:10.1167/iovs.64.14.4

57. Linsenmeier RA, Zhang HF. Retinal oxygen: from animals to humans. Prog Retin Eye Res. 2017;58:115-151. doi:10.1016/j.preteyeres.2017.01.003

58. Chapple SJ, Keeley TP, Mastronicola D, et al. Bach1 differentially regulates distinct Nrf2-dependent genes in human venous and coronary artery endothelial cells adapted to physiological oxygen levels. Free Radic Biol Med. 2016;92:152-162. doi:10.1016/j.freeradbiomed.2015.12.013

59. Keeley TP, Mann GE. Defining Physiological Normoxia for Improved Translation of Cell Physiology to Animal Models and Humans. Physiol Rev. 2019;99:161-234. doi:10.1152/physrev.00041.2017.-The

60. Harmansa S, Hamaratoglu F, Affolter M, Caussinus E. Dpp spreading is required for medial but not for lateral wing disc growth. Nature. 2015;527. doi:10.1038/nature15712

61. Krzystyniak A, Gluchowska A, Mosieniak G, Sikora E. Fiji-Based Tool for Rapid and Unbiased Analysis of SA-β-Gal Activity in Cultured Cells. Biomolecules. 2023;13(2):362. doi:10.3390/biom13020362

62. Burhans WC, Heintz NH. The cell cycle is a redox cycle: Linking phase-specific targets to cell fate. Free Radic Biol Med. 2009;47(9):1282-1293. doi:10.1016/j.freeradbiomed.2009.05.026

63. Cairns RA, Harris IS, Mak TW. Regulation of cancer cell metabolism. Nat Rev Cancer. 2011;11(2):85-95. doi:10.1038/nrc2981

64. Rapkine L. Chemical processes during cellular division. Ann Physiol Physico Chim Biol. 1931;7:382-417.

65. Kaplan N, Urao N, Furuta E, et al. Localized cysteine sulfenic acid formation by vascular endothelial growth factor: role in endothelial cell migration and angiogenesis. Free Radic Res. 2011;45(10):1124-1135. doi:10.3109/10715762.2011.602073

66. Cameron JM, Gabrielsen M, Chim YH, et al. Polarized Cell Motility Induces Hydrogen Peroxide to Inhibit Cofilin via Cysteine Oxidation. Current Biology. 2015;25(11):1520-1525. doi:10.1016/j.cub.2015.04.020

67. Renaud CCN, Nicolau CA, Maghe C, et al. Necrosulfonamide causes oxidation of PCM1 and impairs ciliogenesis and autophagy. iScience. 2024;27(4):109580. doi:10.1016/j.isci.2024.109580

68. Hoehne MN, Jacobs LJHC, Lapacz KJ, et al. Spatial and temporal control of mitochondrial H 2 O 2 release in intact human cells. EMBO J. 2022;41(7):1-16. doi:10.15252/embj.2021109169

69. Salmeen A, Park BO, Meyer T. The NADPH oxidases NOX4 and DUOX2 regulate cell cycle entry via a p53-dependent pathway. Oncogene. 2010;29:4473-4484. doi:10.1038/onc.2010.200

70. van Soest DMK, Polderman PE, den Toom WTF, et al. Mitochondrial H2O2 release does not directly cause damage to chromosomal DNA. Nat Commun. 2024;15(1):2725. doi:10.1038/s41467-024-47008-x

71. Kritsiligkou P, Bosch K, Shen TK, Meurer M, Knop M, Dick TP. Proteome-wide tagging with an H2O2 biosensor reveals highly localized and dynamic redox microenvironments. Proceedings of the National Academy of Sciences. 2023;120(48). doi:10.1073/pnas.2314043120

72. Stöcker S, Van Laer K, Mijuskovic A, Dick TP. The Conundrum of Hydrogen Peroxide Signaling and the Emerging Role of Peroxiredoxins as Redox Relay Hubs. Antioxid Redox Signal. 2018;28(7):558-573. doi:10.1089/ars.2017.7162

73. Kemper EK, Zhang Y, Dix MM, Cravatt BF. Global profiling of phosphorylation-dependent changes in cysteine reactivity. Nat Methods. 2022;19(3):341-352. doi:10.1038/s41592-022-01398-2

74. Kang MA, So EY, Simons AL, Spitz DR, Ouchi T. DNA damage induces reactive oxygen species generation through the H2AX-Nox1/Rac1 pathway. Cell Death Dis. 2012;3(1). doi:10.1038/cddis.2011.134

75. Lindell E, Zhong L, Zhang X. Quiescent Cancer Cells—A Potential Therapeutic Target to Overcome Tumor Resistance and Relapse. Int J Mol Sci. 2023;24(4):3762. doi:10.3390/ijms24043762

76. Nimalasena S, Gothard L, Anbalagan S, et al. Intratumoral Hydrogen Peroxide With Radiation Therapy in Locally Advanced Breast Cancer: Results From a Phase 1 Clinical Trial. International Journal of Radiation Oncology*Biology*Physics. 2020;108(4):1019-1029. doi:10.1016/j.ijrobp.2020.06.022

77. Gu L, Gao W, Yang HM, et al. Control of Trx1 redox state modulates protection against methyl methanesulfonate-induced DNA damage via stabilization of p21. J Biochem. 2016;159(1):101-110. doi:10.1093/jb/mvv080

78. Kolberg L, Raudvere U, Kuzmin I, Adler P, Vilo J, Peterson H. g:Profiler—interoperable web service for functional enrichment analysis and gene identifier mapping (2023 update). Nucleic Acids Res. 2023;51(W1):W207-W212. doi:10.1093/nar/gkad347

79. Jehl P, Manguy J, Shields DC, Higgins DG, Davey NE. ProViz—a web-based visualization tool to investigate the functional and evolutionary features of protein sequences. Nucleic Acids Res. 2016;44(W1):W11-W15. doi:10.1093/nar/gkw265

80. Jeremy M. Berg, Lubert Stryer, John L. Tymoczko, Gregory J. Gatto. Biochemistry. 8th ed. Macmillan Learning; 2015.

81. Clement K, Rees H, Canver MC, et al. CRISPResso2 provides accurate and rapid genome editing sequence analysis. Nat Biotechnol. 2019;37(3):224-226. doi:10.1038/s41587-019-0032-3

82. Peng T, Thorn K, Schroeder T, et al. A BaSiC tool for background and shading correction of optical microscopy images. Nat Commun. 2017;8(1):14836. doi:10.1038/ncomms14836

83. Schmidt U, Weigert M, Broaddus C, Myers G. Cell Detection with Star-Convex Polygons. In: ; 2018:265-273. doi:10.1007/978-3-030-00934-2_30

84. Berg S, Kutra D, Kroeger T, et al. ilastik: interactive machine learning for (bio)image analysis. Nat Methods. 2019;16(12):1226-1232. doi:10.1038/s41592-019-0582-9

85. Ershov D, Phan MS, Pylvänäinen JW, et al. TrackMate 7: integrating state-of-the-art segmentation algorithms into tracking pipelines. Nat Methods. 2022;19(7):829-832. doi:10.1038/s41592-022-01507-1

86. Schindelin J, Arganda-Carreras I, Frise E, et al. Fiji: an open-source platform for biological-image analysis. Nat Methods. 2012;9(7):676-682. doi:10.1038/nmeth.2019

87. Shannon P, Markiel A, Ozier O, et al. Cytoscape: A Software Environment for Integrated Models of Biomolecular Interaction Networks. Genome Res. 2003;13(11):2498-2504. doi:10.1101/gr.1239303

88. Pettersen EF, Goddard TD, Huang CC, et al. UCSF ChimeraX: Structure visualization for researchers, educators, and developers. Protein Science. 2021;30(1):70-82. doi:10.1002/pro.3943

89. Madeira F, Pearce M, Tivey ARN, et al. Search and sequence analysis tools services from EMBL-EBI in 2022. Nucleic Acids Res. 2022;50(W1):W276-W279. doi:10.1093/nar/gkac240